

1 Secondary ice production processes in wintertime alpine 2 mixed-phase clouds

3
4 Paraskevi Georgakaki¹, Georgia Sotiropoulou^{1,2,5}, Étienne Vignon³, Anne-Claire Billault-
5 Roux⁴, Alexis Berne⁴ and Athanasios Nenes^{1,5}

6
7 ¹Laboratory of Atmospheric Processes and their Impacts, School of Architecture, Civil & Environmental
8 Engineering, École Polytechnique Fédérale de Lausanne, Lausanne, CH-1015, Switzerland

9 ²Department of Meteorology, Stockholm University & Bolin Center for Climate Research, Stockholm, Sweden

10 ³Laboratoire de Météorologie Dynamique/IPSL/Sorbonne Université/CNRS, UMR 8539, Paris, France

11 ⁴Environmental Remote Sensing Laboratory, School of Architecture, Civil & Environmental Engineering, École
12 Polytechnique Fédérale de Lausanne, Lausanne, CH-1015, Switzerland

13 ⁵Center for Studies of Air Quality and Climate Change, Institute of Chemical Engineering Sciences, Foundation
14 for Research and Technology Hellas, Patras, GR-26504, Greece

15 *Correspondence to:* athanasios.nenes@epfl.ch

17 Abstract

18 Observations of orographic mixed-phase clouds (MPCs) have long shown that measured ice
19 crystal number concentrations (ICNCs) can exceed the concentration of ice nucleating particles
20 by orders of magnitude. Additionally, model simulations of alpine clouds are frequently found
21 to underestimate the amount of ice compared with observations. Surface-based blowing snow,
22 hoar frost and secondary ice production processes have been suggested as potential causes, but
23 their relative importance and persistence remains highly uncertain. Here we study ice
24 production mechanisms in wintertime orographic MPCs observed during the Cloud and
25 Aerosol Characterization Experiment (CLACE) 2014 campaign at the Jungfrauoch site in the
26 Swiss Alps with the Weather Research and Forecasting model (WRF). Simulations suggest
27 that droplet shattering is not a significant source of ice crystals at this specific location – but
28 break-up upon collisions between ice particles is quite active, elevating the predicted ICNCs
29 by up to 3 orders of magnitude, which is consistent with observations. The initiation of the ice-
30 ice collisional break-up mechanism is primarily associated with the occurrence of seeder-feeder
31 events from higher precipitating cloud layers. The enhanced aggregation of snowflakes is found
32 to drive secondary ice formation in the simulated clouds, the role of which is strengthened
33 when the large hydrometeors interact with the primary ice crystals formed in the feeder cloud.
34 Including a constant source of cloud ice crystals from blowing snow, through the action of the
35 break-up mechanism, can episodically enhance ICNCs. Increases in secondary ice fragment
36 generation can be counterbalanced by enhanced orographic precipitation, which seems to
37 prevent explosive multiplication and cloud dissipation. These findings highlight the importance
38 of secondary ice and “seeding” mechanisms – primarily falling ice from above and to a lesser

39 degree blowing ice from the surface – which frequently enhance primary ice and determine the
40 phase state and properties of MPCs.

41

42 1. Introduction

43 Understanding orographic precipitation is one of the most critical aspects of weather
44 forecasting in mountainous regions (Roe, 2005; Rotunno and Houze, 2007; Chow et al., 2013).
45 Orographic clouds are often mixed-phase clouds (MPCs), containing simultaneously
46 supercooled liquid water droplets and ice crystals (Lloyd et al., 2015; Lohmann et al., 2016;
47 Henneberg et al., 2017). MPCs are persistent in complex mountainous terrain, because the high
48 updraft velocity conditions generate supercooled liquid droplets faster than can be depleted by
49 ice production mechanisms (Korolev and Isaac, 2003; Lohmann et al., 2016). In mid- and high-
50 latitude environments almost all precipitation originates from the ice phase (Field and
51 Heymsfield, 2015; Mülmenstädt et al., 2015), highlightingemphasizing the
52 ~~importance~~necessity of correctly simulating the amount and distribution of both liquid water
53 and ice (i.e., the liquid-ice phase partitioning) in MPCs (Korolev et al., 2017).

54 Our understanding of MPCs remains incomplete owing to the numerous and highly
55 nonlinear cloud microphysical pathways driving their properties and evolution (Morrison et al.,
56 2012). ~~Due to the lower equilibrium water vapor pressure over ice crystals than over liquid
57 water,~~ MPCs tend to glaciate over time through the Wegener-Bergeron-Findeisen (WBF)
58 process, which is the rapid ice crystal growth at the expense of the surrounding evaporating
59 cloud droplets (Bergeron, 1935; Findeisen, 1938). ~~Another process that~~Ice crystals falling from
60 a high-level seeder cloud into a lower-level cloud (external “seeder-feeder” event) or a lower-
61 lying part of the same cloud (in-cloud “seeder-feeder” event) can trigger cloud glaciation and
62 has been shown to enhance precipitation over mountains ~~is the seeder-feeder mechanism~~ (e.g.,
63 Roe, 2005). ~~This mechanism has been observed in several field studies (e.g.,~~ Reinking et al.,
64 2000; Purdy et al., 2005; Mott et al., 2014; Ramelli et al., 2021) ~~and refers to ice crystals falling
65 from a high-level seeder cloud into a lower-level cloud (external seeder-feeder event) or a
66 lower-lying part. Analysis~~ of the same cloud (in-cloud seeder-feeder event), where they act as
67 ~~seeds for the glaciation of clouds. Satellite products covering satellite remote sensing over~~ the
68 11-year period between April 2006 and October 2017 ~~indicated~~suggest that seeding events are
69 widespread over Switzerland, occurring with a frequency of 31% of the total observations in
70 which cirrus clouds seed lower mixed-phase cloud layers (Proske et al., 2021). ~~Despite these
71 two mechanisms that can readily destabilize an orographic cloud, a high frequency of MPCs~~

Formatted: French (Switzerland)

72 ~~have been reported under high updraft velocity conditions prevailing over the complex~~
73 ~~mountainous terrain (e.g., in the Swiss Alps), where supercooled liquid droplets are generated~~
74 ~~faster than depleted by depositional ice growth and riming, leading to persistent mixed phase~~
75 ~~conditions (Korolev and Isaac, 2003; Lohmann et al., 2016).~~

76 ~~At temperatures between 0 °C and -38 °C, where mixed phase conditions can occur,~~
77 ~~primary ice formation in clouds is catalyzed by the presence of insoluble aerosols that act as,~~

78 Primary ice formation in MPCs is catalyzed by the action of ice nucleating particles
79 (INPs) (e.g., Hoose and Möhler, 2012, Kanji et al., 2017). However, in-situ observations of
80 MPCs ~~forming over mountain top research stations or near mountain slopes in orographic~~
81 environments regularly reveal that ~~there is a mismatch between the scarcity of primary INPs~~
82 ~~and the measured ice crystal number concentrations (ICNCs) —the latter being are~~ several
83 orders of magnitude more abundant than INPs (Rogers and Vali, 1987; Geerts et al., 2015;
84 Lloyd et al., 2015; Beck et al., 2018; Lowenthal et al., 2019; Mignani et al., 2019). Model
85 simulations of alpine MPCs frequently fail to reproduce the elevated ICNCs dictated by
86 observations (Farrington et al., 2016; Henneberg et al., 2017; Dedekind et al., 2021).

87 The ~~fact that inability of~~ primary ice ~~cannot explain to reproduce~~ the observed ICNCs in
88 orographic MPCs has often been attributed to the influence of surface processes ~~such as~~
89 ~~the including~~ lofting of snowflakes (i.e., “blowing snow”; Rogers and Vali, 1987; Geerts et al.,
90 2015), detachment of surface hoar frost (Lloyd et al., 2015), turbulence near the mountain
91 surface or convergence of ice particles due to orographic lifting (Beck et al., 2018) and riming
92 on snow-covered surfaces (Rogers and Vali, 1987). The impact of blowing snow ice particles
93 (BIPS) has been studied thoroughly, either using observations collected in mountainous regions
94 (e.g., Lloyd et al., 2015; Beck et al., 2018; Lowenthal et al., 2019), remote sensing (e.g., Rogers
95 and Vali, 1987; Vali et al., 2012; Geerts et al., 2015) or detailed snow-cover models (e.g.,
96 Lehning et al., 2006; Krinner et al., 2018) coupled with atmospheric models (e.g., Vionnet et
97 al., 2014; Sharma et al., 2021. The extent to which BIPS can affect ICNCs in MPCs remains
98 poorly understood.

99 ~~Among these surface processes, the~~In-cloud secondary ice production (SIP) – or ice
100 multiplication – processes may also enhance ice production above the concentration of INPs
101 (Field et al., 2017; ~~impact of blowing snow ice particles (BIPS) has been studied thoroughly,~~
102 either using observations collected in mountainous regions (e.g., Lloyd et al., 2015; Beck et
103 al., 2018; Lowenthal et al., 2019), and detailed surface snow models (e.g., Lehning et al., 2006;
104 Vionnet et al., 2013, 2014) or through remote sensing techniques (e.g., Rogers and Vali, 1987;
105 Vali et al., 2012; Geerts et al., 2015). BIPS are found to hover close to the surface provided

106 that the wind speed exceeds a threshold value, which varies between 4 and 13 ms⁻¹ (e.g., Déry
107 and Yau, 1999; Mahesh et al., 2003), depending on the snowpack properties and the prevailing
108 atmospheric conditions. The transport of BIPS is commonly separated into the saltation layer
109 and the turbulent suspension layer. The saltation layer is a shallow layer formed close to the
110 ground, where the transported ice particles are found to follow ballistic trajectories. Turbulent
111 eddies or upward gusts can then diffuse the saltated ice particles up to a height of several tens
112 of meters above the surface, into the suspension layer (e.g., Vali et al., 2012; Vionnet et al.,
113 2014).

114 In cloud secondary ice production (SIP) processes may also enhance ice production after
115 the initial primary ice nucleation events. Especially for orographic clouds, whose cloud top
116 temperatures are not cold enough to activate sufficient INPs, ice multiplication through SIP
117 might be particularly important. Over the past few decades, several SIP mechanisms have
118 emerged in literature, a detailed review of which is provided by Field et al. (2017) and Korolev
119 and Leisner (2020). We briefly review the three main SIP mechanisms below:

120 are thought to be responsible for most of the SIP. The rime splintering, also first, known
121 as the Hallett-Mossop (HM) process (Hallett and Mossop, 1974), is argued to be the most
122 efficient one in slightly supercooled clouds (i.e., temperatures warmer than -10 °C). The HM
123 process refers to the ejection of small secondary ice splinters after a supercooled droplet with
124 a diameter larger than ~25 μm rimes onto a large ice particle at temperatures between -8 and -
125 3 °C (Choulaton et al., 1980; Heymsfield and Mossop, 1984). Although this is the only This
126 SIP mechanism is widely implemented in current microphysics schemes atmospheric models
127 (e.g., Beheng, 1987; Phillips et al., 2001; Morrison et al., 2005), recent modeling studies of
128 slightly supercooled polar clouds, have shown that it cannot sufficiently but cannot on its own
129 explain the enhanced ICNCs in remote environments (Young et al., 2019; Sotiropoulou et al.,
130 2020, 2021a). Moreover, aircraft measurements have reported high ICNCs, especially for when
131 the conditions required for HM initiation are not fulfilled (e.g., Korolev et al., 2020).

132 A second process that is found to contribute to ice multiplication over a wider
133 temperature range is the collisional Collisional fracturing and breakup (BR), which involves the
134 fracturing of delicate ice particles due to collisions with other ice particles (Vardiman, 1978;
135 Griggs and Choulaton, 1986; Takahashi et al., 1995). Evidence for this process is provided
136 from several is another important SIP mechanism. Several field studies in the Arctic (Rangno
137 and Hobbs, 2001; Schwarzenboeck et al., 2009) or in the Alps (Mignani et al., 2019; Ramelli
138 et al., 2021) and from limited laboratory investigations (Vardiman 1978; Takahashi et al. 1995).
139 These 1995 all show the importance of BR. The latter two studies created a the basis for various

Field Code Changed

140 ~~numerical formulations of the BR mechanism~~ a mechanistic description of BR (e.g., Phillips et
141 al., 2017a; Sullivan et al., 2018a; Sotiropoulou et al., 2020). Parameterizations of ~~this~~
142 ~~mechanism are~~ BR have recently been implemented in small-scale ~~models~~ (Fridlind et al., 2007;
143 Phillips et al., 2017a, b; Sotiropoulou et al., 2020, 2021b; Sullivan et al., 2018a; Yano and
144 Phillips, 2011; Yano et al., 2016), mesoscale ~~models~~ (Hoarau et al., 2018; Sullivan et al.,
145 2018b; Qu et al., 2020; Sotiropoulou et al., 2021a; Dedekind et al., 2021) and global climate
146 models (Zhao and Liu, 2021a). ~~These modeling studies followed several approaches to~~
147 ~~implement the effect of BR. For instance, Hoarau et al. (2018) assumed a constant number of~~
148 ~~fragments generated per collision in the Meso-NH model, while Sullivan et al. (2018b)~~
149 ~~implemented a temperature dependent relationship in the COSMO-ART mesoscale model~~
150 ~~based on the results of Takahashi et al. (1995). This simplified formulation was further~~
151 ~~modified to account for the hydrometeor size scaling, which improved the representation of~~
152 ~~ICNCs in alpine clouds (Dedekind et al., 2021). Sotiropoulou et al. (2020) and (2021a)~~
153 ~~reproduced the observed ICNCs in polar clouds, by applying the physically based~~
154 ~~parameterization developed by Phillips et al. (2017a, b). At slightly colder temperatures~~
155 ~~(between -12.5 °C and -7 °C), however, BR was found to be generally weak over the Arctic~~
156 ~~(Sotiropoulou et al., 2021b; Zhao et al., 2021).~~ each with their own approach towards BR
157 description.

158 Droplet freezing and shattering (DS) during freezing is a third ~~process that is frequently~~
159 ~~suggested to explain the unexpected ice enhancement in clouds. This~~ SIP mechanism that can
160 produce significant amounts of ice crystals. It occurs when ~~a drizzle-sized droplet, with a size~~
161 drops (diameter larger than ~exceeding 50 µm collides) comes in contact with an ice particle
162 or INP, ~~triggering its freezing after a~~ A solid ice shell is initially formed around the droplet
163 (e.g., Griggs and Choulaton, 1983). ~~As the freezing moves inward, the pressure starts to build~~
164 ~~and the freezing droplet reacts by either, and as it thickens begins building up pressure that~~
165 leads to breakup in two halves, cracking, bubble burst or jetting (e.g., Keinert et al., 2020).
166 ~~These processes may be accompanied by the ejection~~ Ejection of small ice fragments may
167 occur, the number of which ~~is yet poorly constrained as recent laboratory studies are showing~~
168 a large diversity of results varies considerably (Lauber et al., 2018; Keinert et al., 2020;
169 Kleinheins et al., 2021; James et al., 2021). ~~Individual experiments of freezing droplets~~
170 ~~reported the maximum~~ Experimentally, fragmentation rate maximizes at temperatures between
171 ~ -10 and -15 °C (Leisner et al., 2014; Lauber et al., 2018; Keinert et al., 2020). ~~DS is found~~
172 to be very efficient can dominate in ~~vigorous~~ convective updrafts (Lawson et al., 2015; Phillips
173 et al., 2018; Korolev et al., 2020; Qu et al., 2020), ~~while remote~~ Remote sensing observations

Formatted: French (Switzerland)

174 ~~indicate that of warm Arctic MPCs suggest~~ DS can be much more conducive to SIP ~~in slightly~~
175 ~~supercooled Arctic MPCs than the well known~~ HM process (Luke et al., 2021). ~~This is in line~~
176 ~~with single~~Single-column simulations ~~performed~~ by Zhao et al. (2021) ~~support this~~, but
177 ~~contradicts the findings of is in contrast with~~ small-scale modeling studies ~~suggesting that DS~~
178 ~~is ineffective in polar regions~~ (Fu et al., 2019; Sotiropoulou et al., 2020). Mesoscale model
179 simulations of winter alpine clouds formed at temperatures lower than -8°C indicate that DS
180 is not ~~contributing to the modeled ICNCs~~active (Dedekind et al., 2021), while field
181 observations suggest the increasing efficiency of the mechanism at temperatures warmer than
182 -3°C (Lauber et al., 2021).

183 ~~In the orographic MPCs observed~~Orographic ICNCs in MPCs exceeded the predicted
184 ~~INPs by 3 orders of magnitude, reaching up to $\sim 1000\text{ L}^{-1}$ at -15°C~~ during the Cloud and
185 Aerosol Characterization Experiment (CLACE) 2014 campaign at the ~~high altitude research~~
186 ~~station of Jungfrauoch (JFJ) station~~ in the Swiss Alps, ~~the measured ICNCs exceeded the~~
187 ~~predicted INPs by 3 orders of magnitude, reaching up to $\sim 1000\text{ L}^{-1}$ at temperatures around -15~~
188 ~~$^{\circ}\text{C}$ (Lloyd et al. 2015). Whilst ice multiplication through~~Although the efficiency of BR and
189 DS ~~mechanisms show a peak production~~peaks at around ~~a similar~~the same temperature, Lloyd
190 et al. (2015) did not find evidence for their occurrence. Instead, ~~they suggested that~~ at periods
191 when there was a strong correlation between horizontal wind speed and observed ICNCs, ~~ICNC~~
192 ~~they suggested that~~ BIPS is contributing to the latter, but ~~the mechanism was incapable of~~
193 ~~producing ICNCs higher than~~could not get ICNCs to exceed $\sim 100\text{ L}^{-1}$. In the absence of such
194 correlation, a flux of hoar frost crystals was considered responsible for the very high ice
195 concentration events (ICNCs $> 100\text{ L}^{-1}$), albeit without any direct evidence. ~~Beek et al. (2018)~~
196 ~~argued that the relationship between ICNCs and horizontal wind speed may not be a good~~
197 ~~indicator for distinguishing between blowing snow and hoar frost. Their measurements~~
198 ~~conducted at the Sonnblick Observatory in the Austrian Alps revealed the presence of several~~
199 ~~hundred ice crystals of blowing snow per liter during cloud free conditions. In a cloudy~~
200 ~~environment, though, such high contribution from BIPS was found only close to the surface,~~
201 ~~with the concentrations dropping to several tens to 100 L^{-1} at heights above $\sim 10\text{ m}$.~~

202 From a modeling perspective, the causes of the surprisingly high ICNCs in orographic
203 MPCs formed during the CLACE 2014 campaign were explored in Farrington et al. (2016).
204 Since temperatures at JFJ are generally outside the HM temperature range ($\ll -8^{\circ}\text{C}$), Farrington
205 et al. (2016) used back trajectories analysis to investigate whether splinters produced at lower
206 altitudes through the HM process could be lifted to the summit of JFJ elevating the modeled
207 ICNCs. They Farrington et al. (2016) showed that the inclusion of the HM process upwind of

208 JFJ could not explain the measured concentrations of ice, while the addition of a surface flux
209 of hoar crystals provided the best agreement with observations.

210 Although surface-originated processes have been frequently invoked to explain the
211 disparity between ICNCs and INPs, the role of SIP processes – especially the BR and the DS
212 mechanism – has received ~~much~~far less attention. ~~In and is addressed in~~ this study ~~we~~. We
213 utilize the Weather Research and Forecasting model (WRF) to conduct simulations of two case
214 studies observed in winter during the CLACE 2014 campaign. Our primary objective is to
215 investigate if the implementation of two SIP parameterizations that account for the effect of
216 BR and DS can reduce the discrepancies between observed and simulated ICNCs. Additionally,
217 we aim to identify the conditions favoring the initiation of SIP in the orographic terrain and
218 explore the synergistic influence of SIP with wind-blown ice.

219

220 2. Methods

221 2.1 CLACE instrumentation

222 CLACE is a long-established series of campaigns taking place for over two decades at the
223 mountain-top station of JFJ, located in the Bernese Alps, in Switzerland, at an altitude of ~3580
224 m above sea level (a.s.l.) (e.g., Choularton et al., 2008). The measurement area is very complex
225 and heterogeneous with distinct mountain peaks (Fig. 1), while JFJ is covered by clouds
226 approximately 40% of the time, offering an ideal location for microphysical observations
227 (Baltensperger et al., 1998). Owing to the local orography surrounding the site, the wind flow
228 is constrained to two directions (Ketterer et al., 2014). Under southeasterly (SE) wind
229 conditions, air masses are lifted along the moderate slope of the Aletsch Glacier, whereas under
230 northwesterly (NW) wind conditions the air is forced to rise faster along the steep north face
231 of the Alps, which is associated with persistent MPCs (Lohmann et al., 2016). A detailed
232 description of the in-situ and remote sensing measurements taken during January and February
233 2014 as part of the CLACE 2014 campaign is provided by Lloyd et al. (2015) and Grazioli et
234 al. (2015). Here we only offer a brief presentation of the datasets used in this study.

235 Shadowgraphs of cloud particles were produced by the two-dimensional stereo
236 hydrometeor spectrometer (2D-S; Lawson et al., 2006), part of a three-view cloud particle
237 imager (3V-CPI) instrument. The 2D-S products have been used to provide information on the
238 number concentration and size distribution of particles in the size range of 10-1280 μm .
239 Following Crosier et al. (2011), the raw data were ~~further~~ processed to ~~determine~~
240 ~~between~~distinguish ice crystals ~~and~~from droplets, ~~and to remove~~. Removal of artefacts from

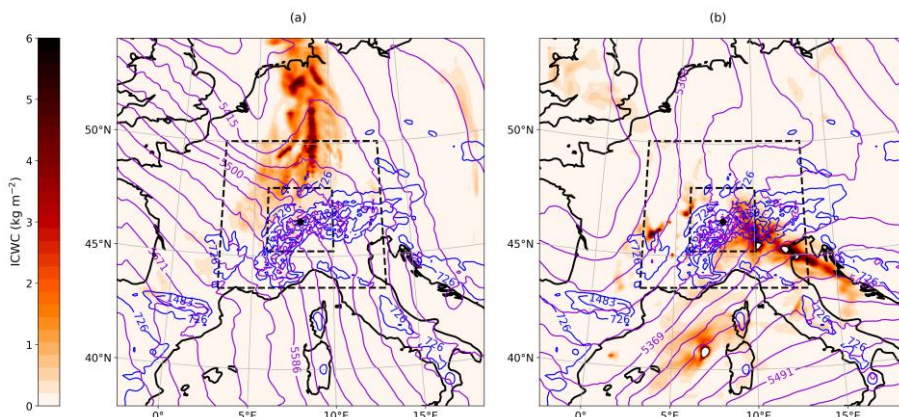
241 shattering events was also considered (Korolev et al., 2011); however analysis of the probe
242 imagery (Crosier et al., 2011) along with inter-arrival time histograms did not reveal the
243 presence of shattered particles, presumably because of the much lower velocity at which the
244 2D-S probe was aspirated ($\sim 15 \text{ ms}^{-1}$) compared to those during aircraft deployments (Lloyd et
245 al., 2015). An approximation of the ice water content (IWC) at JFJ could also be derived by
246 the 2D-S data using the Brown and Francis (1995) mass-diameter relationship with a factor an
247 uncertainty of up to 5 uncertainty times (Heymsfield et al., 2010). Additionally, the
248 quantification of the liquid water content (LWC) is based on the liquid droplet size distribution
249 data derived from a DMT cloud droplet probe (CDP; Lance et al., 2010) over the size range
250 between 2 and 50 μm . ~~Typical meteorological~~ Meteorological parameters (e.g., temperature,
251 relative humidity, wind speed and wind direction), ~~that served as comparison to assess the~~
252 ~~validity of the model,~~ were provided by ~~the weather station managed by~~ MeteoSwiss at JFJ.
253 The instrumentation was set up on the roof terrace outside the Sphinx laboratory and used to
254 evaluate the model.

256 2.2 WRF simulations

257 ~~WRF model,~~ version 4.0.1, with augmented cloud microphysics to include the effects of all
258 SIP mechanisms (Sotiropoulou et al., 2021a) is used for non-hydrostatic cloud-resolving
259 simulations. The model has been run with three two-way nested domains (Fig. 1), with a
260 respective horizontal resolution of 12, 3 and 1 km. Two-way grid nesting is generally found to
261 improve the model performance in the inner domain (e.g., Harris and Durran, 2010), although
262 the sensitivity of the results to the applied nesting technique has been shown to be negligible
263 (not shown). The parent domain consists of 148×148 grid points centered over the JFJ station
264 (46.55°N , 7.98°E , shown with a black dot in Fig. 1), while the second and the third domain
265 include 241×241 and 304×304 grids, respectively. The Lambert conformal projection is
266 applied to all three domains, as it is well-suited for mid-latitudes. Here we adapted the so-called
267 “refined” vertical grid spacing proposed by Vignon et al. (2021), using 100 vertical eta levels
268 up to a model top of 50 hPa (i.e., ~ 20 km). This set-up provides a refined vertical resolution of
269 ~ 100 m up to mid-troposphere at the expense of the coarsely resolved stratosphere. To
270 investigate the dynamical influence on the development of MPCs under the two distinct wind
271 regimes prevailing at JFJ (Section 2.1), we simulate two case studies, starting on 25 January
272 and 29 January 2014, 00:00 UTC, respectively. Both case studies are associated with the
273 passage of frontal systems over the region of interest, approaching the alpine slopes either from

274 the NW (cold front) or the SE (warm front) direction, as shown by the vertically-integrated
 275 condensed water content (ICWC; sum of cloud droplets, rain, cloud ice, snow, and graupel) in
 276 Fig. 1. For both cases the simulation covers a 3-day period, with the first 24 hours being
 277 considered sufficient time for spin up. A 27-s time step was used in the parent domain and goes
 278 down to 9 s in the second domain and 3 s in the third domain. Note that achieving such small
 279 time steps in the innermost domain is essential to ensure numerical stability in non-hydrostatic
 280 simulations over a region with complex orography such as around JFJ.

281



282

283 **Figure 1.** Map of synoptic conditions around JFJ station at (a) 00:00 UTC, 26 January 2014
 284 and (b) 00:00 UTC, 30 January 2014, from the control simulation (12-km resolution domain).
 285 The purple (blue) contours show the 500 hPa geopotential height in m (the terrain heights in
 286 m). The color shading shows the vertically-integrated condensed water content (in kg m^{-2}). The
 287 black dashed lines delimit the 3-km and 1-km resolution domains, while the black dot locates
 288 the JFJ station.

289

290 The ERA5 reanalysisThe fifth generation of the European Centre for Medium-Range
 291 Weather Forecasts (ECMWF) atmospheric reanalyses dataset (ERA5; Hersbach et al., 2020) is
 292 used to initialize the model and provide the lateral forcing at the edge of the 12-km resolution
 293 domain every 6 hours. Static fields at each model grid point come from default WRF pre-
 294 processing system datasets, with a resolution of 30" for both the topography and the "land
 295 use" use fields. The MODIS-Land use categories are based ~~dataset is used foron the Moderate~~
 296 Resolution Imaging Spectroradiometer (MODIS) land-cover classification. Regarding the
 297 physics options chosen to run WRF simulations, the Rapid Radiative Transfer Model for
 298 general circulation models (RRTMG) radiation scheme is applied to parameterize both the
 299 short-wave and long-wave radiative transfer. The vertical turbulent mixing is treated with the

300 Mellor-Yamada-Janjic (MYJ; Janjić, 2002) 1.5 order scheme, while surface options are
301 modeled by the Noah land-surface model (Noah LSM; Chen and Dudhia, 2001). The Kain-
302 Fritsch cumulus parameterization has been activated only in the outermost domain, as the
303 resolution of the two nested domains is sufficient to reasonably resolve cumulus-type clouds
304 at grid-scale.

305

306 2.2.1 Microphysics scheme and primary ice production

307 The Morrison two-moment scheme (Morrison et al., 2005; hereafter M05) is used to
308 parameterize the cloud microphysics, following the alpine cloud study of Farrington et al.
309 (2016). The scheme includes double-moment representations of rain, cloud ice, snow and
310 graupel species, while cloud droplets are treated with a single-moment approach and therefore
311 the [cloud](#) droplet number concentration (N_d) must be prescribed. Here N_d is set to 100 cm^{-3} ,
312 based on the mean N_d observed within the simulated temperature range (Lloyd et al., 2015).

313 Three primary ice production mechanisms through heterogeneous nucleation are
314 described in the default version of the M05 scheme, namely immersion freezing, contact
315 freezing, and deposition/condensation freezing nucleation. Immersion freezing of cloud
316 droplets and raindrops is described by the probabilistic approach of Bigg (1953). Contact
317 freezing is parameterized following Meyers et al. (1992). Finally, deposition and condensation
318 freezing is represented by the temperature-dependent equation derived by Rasmussen et al.
319 (2002) based on the in-situ measurements of Cooper (1986) collected from different locations
320 at different temperatures. Following Thompson et al. (2004), this parameterization is activated
321 either when there is saturation with respect to liquid water and the simulated temperatures are
322 below $-8 \text{ }^\circ\text{C}$ or when the saturation ratio with respect to ice exceeds a value of 1.08. The
323 accuracy of these parameterizations in representing atmospheric INPs is debatable as they are
324 derived from very localized measurements over a limited temperature range. Nevertheless,
325 Farrington et al. (2016) argued that the deposition/ condensation freezing parameterization of
326 Cooper (1986) can effectively explain INPs between the range 0.01 and 10 L^{-1} , which is
327 frequently observed during field campaigns at JFJ (Chou et al., 2011; Conen et al., 2015).

328

329 2.2.2 Ice multiplication through rime splintering in the M05 scheme

330 Apart from primary ice production, the HM process is the only SIP mechanism included in the
331 default version of the M05 scheme. This parameterization adapted from Reisner et al. (1998),
332 based on the laboratory findings of Hallett and Mossop (1974), allows for $-$ splinter production

333 after cloud- or rain- drops are collected by rimed snow particles or ~~graupels~~graupel. The
 334 efficiency of this process is zero outside the temperature range between -8 and -3 °C, while it
 335 follows a linear temperature-dependent relationship in between. HM is not activated unless the
 336 rimed ice particles have masses larger than 0.1 g kg^{-1} and cloud or rain mass mixing ratio
 337 exceeds the value of 0.5 g kg^{-1} or 0.1 g kg^{-1} , respectively. Since these conditions are rarely met
 338 in natural MPCs, previous modeling studies had to artificially remove any thresholds to achieve
 339 an enhanced efficiency of this process (Young et al., 2019; Atlas et al., 2020). In the current
 340 study, however, the HM process is not effective, as the simulated temperatures at JFJ altitude
 341 are below -8 °C (see Sect. 2.3).

342

343 2.2.3 Ice multiplication through ice-ice collisions in the M05 scheme

344 In addition to the HM process, we have also included two parameterizations to represent the
 345 BR mechanism. An extensive description of the implementation method is provided in
 346 Sotiropoulou et al. (2021a) (see their Appendix B). Among the three ice particle types included
 347 in the M05 scheme (i.e., cloud ice, snow, graupel), we assume that only the collisions between
 348 cloud ice-snow, cloud ice-graupel, graupel-snow, snow-snow, and graupel-graupel can result
 349 in ice multiplication. The first parameterization tested here follows the simplified methodology
 350 proposed by Sullivan et al. (2018a), which is based on the laboratory work of Takahashi et al.
 351 (1995). Their findings revealed a strong temperature dependence of the fragment numbers
 352 generated per collision (N_{BR}):

$$N_{BR} = 280 (T - T_{min})^{1.2} e^{-(T-T_{min})/5}, \quad (1)$$

353 where $T_{min} = 252 \text{ K}$, is the minimum temperature for which BR occurs. Yet their experimental
 354 set-up was rather simplified involving only collisions between large hail-sized ice spheres with
 355 diameters of ~ 2 cm. Taking this into account, Sotiropoulou et al. (2021a) further scaled the
 356 temperature-dependent formulation for size:

$$N_{BR} = 280 (T - T_{min})^{1.2} e^{-(T-T_{min})/5} \frac{D}{D_0}, \quad (2)$$

357 where D is the size in meters of the particle that undergoes break-up and $D_0=0.02 \text{ m}$ is the size
 358 of the hail-sized balls used in the experiments of Takahashi et al. (1995).

359 Phillips et al. (2017a) proposed a more physically-based formulation, developing an
 360 energy-based interpretation of the experimental results conducted by Vardiman (1978) and
 361 Takahashi et al. (1995). The initial collisional kinetic energy is considered as the governing
 362 constraint driving the BR process. Moreover, the predicted N_{BR} depends on the ice particle type

363 and morphological habit and is a function of the temperature, particle size and rimed fraction.
 364 Here the generated fragments per collision are described as follows:

$$N_{BR} = aA \left(1 - \exp \left\{ - \left[\frac{CK_0}{aA} \right]^\gamma \right\} \right), \quad (3)$$

365 where $K_0 = \frac{1}{2} \frac{m_1 m_2}{m_1 + m_2} (\Delta u_{n12})^2$ is the initial kinetic energy, in which m_1 and m_2 are the masses
 366 of the colliding particles and $|\Delta u_{n12}| = \{(1.7 u_{n1} - u_{n2})^2 + 0.3 u_{n1} u_{n2}\}^{1/2}$ is the difference
 367 in their terminal velocities. The correction term is proposed by Mizuno et al. (1990) and Reisner
 368 et al. (1998) to account for underestimates when $u_{n1} \approx u_{n2}$. The parameter a in Eq. 3 is the
 369 surface area of the smaller ice particle (or the one with the lower density), defined as $a = \pi D^2$,
 370 with D as in Eq. 2. A in Eq. 3 represents the number density of breakable asperities on the
 371 colliding surfaces. For collisions that involve cloud ice and snow particles A is described as
 372 $A = 1.58 \times 10^7 (1 + 100\Psi^2) \left(1 + \frac{1.33 \times 10^{-4}}{D^{1.5}} \right)$, where $\Psi < 0.5$ is the rimed fraction of the most
 373 fragile ice particle. For graupel-graupel collisions A is given by a temperature-dependent
 374 equation as $A = \frac{a_0}{3} + \max \left(\frac{2a_0}{3} - \frac{a_0}{9} |T - 258|, 0 \right)$, in which $a_0 = 3.78 \times 10^4 \left(1 + \frac{0.0079}{D^{1.5}} \right)$. C
 375 is the asperity-fragility coefficient, which is empirically derived to account for different
 376 collision types, while the exponent γ is equal to 0.3 for collisions between graupel-graupel and
 377 is calculated as a function of the rimed fraction for collisions including cloud ice and snow.
 378 The parameterization was developed based on particles with diameters $500 \mu\text{m} < D < 5 \text{mm}$,
 379 however Phillips et al. (2017a) suggest that it can be used for particle sizes outside the
 380 recommended range as long as the input variables to the scheme are set to the nearest limit of
 381 the range. Finally, since N_{BR} was never observed to exceed 100 in the experiments of Vardiman
 382 (1978), here we also use this value as an upper limit for all collision types (Phillips et al.,
 383 2017a). All predicted fragments emitted through BR are added to the cloud ice category.

384

385 2.2.4 Ice multiplication through droplet shattering in the M05 scheme

386 Two different parameterizations are implemented in the M05 scheme to investigate the
 387 potential efficiency of the DS mechanism in producing secondary ice splinters (N_{DS}). Phillips
 388 et al. (2018) proposed two possible modes of raindrop-ice collisions, that can initiate the
 389 freezing process. In the first mode, the freezing of the drop occurs either by collecting a small
 390 ice particle or through heterogeneous freezing. In the default M05 scheme, the product of ~~the~~
 391 collisions between raindrops and cloud ice is considered to be graupel (snow) – if the rain
 392 mixing ratio is greater (lower) than 0.1 g kg^{-1} , following Reisner et al. (1998). Additionally,

393 the heterogeneous freezing of big raindrops in ~~the~~ immersion mode follows Bigg's (1953)
 394 parameterization (Section 2.2.1). Here we consider that the product of these two processes can
 395 undergo shattering and generate numerous ice fragments, the number of which is parameterized
 396 after Phillips et al. (2018). The formulation is derived by fitting ~~to a pooled dataset~~
 397 ~~from multiple~~ laboratory ~~studies and is given as datasets to~~ a Lorentzian function of temperature
 398 and a polynomial expression of the drop size. More precisely, ~~in the first mode of the~~
 399 ~~formulation~~, the total number of fragments (N) generated per frozen drop are given by:

$$N = \mathcal{E}(D_r)\Omega(T) \left[\frac{\zeta\eta^2}{(T-T_0)^2 + \eta^2} + \beta T \right], \quad (4)$$

400 where T is the temperature (in K) and D_r is the size of the freezing raindrop (in mm). Note that
 401 N is defined as the sum of the big fragments (N_B) and tiny splinters (N_T). Equation (4) applies
 402 only to drop diameters less than 1.6 mm, which is the maximum observed experimentally. For
 403 droplet sizes beyond this maximum value, N can be inferred by linear extrapolation. N_B is
 404 described by another Lorentzian:

$$N_B = \min \left\{ \mathcal{E}(D_r)\Omega(T) \left[\frac{\zeta_B\eta_B^2}{(T-T_{B,0})^2 + \eta_B^2} \right], N \right\}. \quad (5)$$

405 The factors $\mathcal{E}(D_r)$ and $\Omega(T)$ in Eq. (4) and (5) are cubic interpolation functions, ~~preventing the~~
 406 ~~onset of impeding~~ DS for $D_r < 0.05$ mm and $T > -3$ °C. Furthermore, the parameters ζ , η , T_0 , β ,
 407 ζ_B , η_B , $T_{B,0}$, ~~found in these relationships, are derived from previous laboratory studies and~~ are
 408 analytically described in Phillips et al. (2018). ~~Note that~~ ~~That~~ the big fragments emitted (i.e.,
 409 N_B) will be initiated in the model as graupel, snow or frozen drops, while ~~it is only the tiny~~
 410 splinters ($N_T = N - N_B$) ~~that~~ are considered secondary ice (i.e., $N_{DS} = N_T$) ~~and will be~~ passed
 411 to the cloud ice category.

412 The second mode of raindrop-ice collisions includes the accretion of raindrops on impact
 413 with more massive ice particles, such as snow or graupel, the description of which in the M05
 414 scheme is adapted from Ikawa and Saito (1991). ~~This mode has been studied only once in the~~
 415 ~~laboratory~~ ~~While there is only one dedicated laboratory study of this SIP mode (James et al.~~
 416 ~~2021), it was also indirectly investigated in the experimental~~ study of Latham and Warwicker
 417 (1980), who reported that the collision of supercooled raindrops with hailstones can ~~potentially~~
 418 ~~stimulate~~ ~~generate~~ secondary ice. ~~Since there was no quantitative observation of this mode,~~
 419 Phillips et al. (2018) proposed an empirical, energy-based formulation to account for the tiny
 420 splinters ejected after collisions between raindrops and large ice particles:

$$N_{DS} = 3\Phi(T) \times [1 - f(T)] \times \max(DE - DE_{crit}, 0), \quad (6)$$

421 where $DE = \frac{K_0}{S_e}$, is the dimensionless energy given as the ratio of the initial kinetic energy (K_0 ;
422 described in 2.2.3) over the surface energy, which is expressed by the product $S_e = \gamma_{liq}\pi D_r^2$,
423 in which $\gamma_{liq}=0.073$ J m⁻², is the surface tension of liquid water. The critical value of DE used
424 in Eq. (6) for the onset of splashing upon impact is set to $DE_{crit} = 0.2$. The parameter $f(T) =$
425 $-c_w T/L_f$, represents the initial frozen fraction of a supercooled drop during the first stage of
426 the freezing process, where $C_w = 4200$ J kg⁻¹ K⁻¹, is the specific heat capacity of liquid water,
427 $L_f = 3.3 \times 10^5$ J kg⁻¹, is the specific latent heat of freezing, while T is the initial freezing
428 temperature (°C) of the raindrop. Finally, $\Phi(T) = \min[4f(T), 1]$ is an empirical fraction, which
429 represents the probability of any new drop in the splash products to contain a frost secondary
430 ice particle. At temperatures ~ -10 °C this formulation yields $\Phi = 0.5$, meaning that the
431 probability of a secondary drop to contain ice is 50%. ~~The first laboratory investigation of this~~
432 ~~rather uncertain parameter as a function of temperature is provided in~~ James et al. (2021)-
433 ~~provided the first laboratory study to constrain this parameter.~~ Further details regarding the
434 derivation of the empirical parameters and the uncertainties underlying the mathematical
435 formulations are discussed in Phillips et al. (2018).

436 ~~Following Sullivan et al. (2018a), the~~The second DS parameterization tested in this study
437 ~~was developed by Sullivan et al. (2018a) and~~ is ~~described as the product of a polynomial~~
438 ~~expression function~~ of the freezing droplet ~~size (Lawson et al., 2015)~~diameter (D_r in μm), a
439 shattering probability (p_{sh}) and a freezing probability (p_{fr}):

$$N_{DS} = 2.5 \times 10^{-11} (D_r)^4 p_{sh} p_{fr} . \quad (7)$$

440 ~~The diameter dependence describing the fragment numbers generated per fractured frozen~~
441 ~~droplet is derived by nudging the liquid water and ice particle size distributions in one-~~
442 ~~dimensional cloud model simulations towards aircraft observations collected in tropical~~
443 ~~cumulus clouds (Lawson et al., 2015).~~ The p_{sh} is based upon droplet levitation experiments
444 shown in Leisner et al. (2014) and is represented by a temperature-dependent Gaussian
445 distribution, centered at ~ -15 °C. Note that p_{sh} is non-zero only for droplets with sizes greater
446 than 50 μm . The p_{fr} is 0 for temperatures warmer than -3 °C and 1 if temperatures fall below $-$
447 6 °C, following the cubic interpolation function, $\Omega(T)$, adapted from Phillips et al. (2018).

448

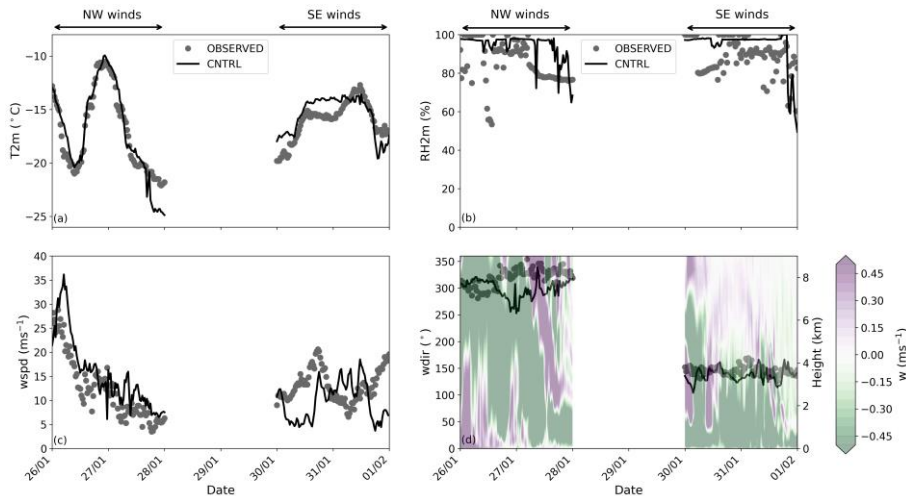
449 2.3 Model validation

450 The control simulation (CNTRL), performed with the standard M05 scheme, sets the basis for
451 assessing the validity of the model against available meteorological observations. Temperature,

452 relative humidity, wind speed, and wind direction are obtained from the MeteoSwiss weather
 453 station at JFJ. The comparison of each meteorological variable with the results from the nearest
 454 model grid point of the CNTRL simulation is shown in Fig. 2. Note that the outputs are from
 455 the first atmospheric level of the innermost domain at ~10 m above ground level (a.g.l) (Fig.
 456 1), while the first 24 hours of each simulation period are considered spin up time and are
 457 therefore excluded from the present analysis. The mean modeled values and standard
 458 deviations (std), along with the root mean square error (RMSE) and the index of agreement
 459 (IoA) between model predictions and observational data are summarized in Table 1. IoA is
 460 both a relative and a bounded measure (i.e., $0 \leq \text{IoA} \leq 1$) that describes phase errors between
 461 predicted (P_i) and observed (O_i) time series (Willmott et al., 2012):

$$\text{IoA} = 1 - \left[\frac{\sum_{i=1}^N (P_i - O_i)^2}{\sum_{i=1}^N (|P_i| + |O_i|)^2} \right], \quad (8)$$

462 where $P'_i = P_i - \bar{O}$ and $O'_i = O_i - \bar{O}$, in which \bar{O} is the mean of the observed variable.
 463



464 **Figure 2.** Time series of (a) temperature (T2m), (b) relative humidity with respect to liquid
 465 phase at 2m height (RH2m), (c) wind speed (wspd) and (d) wind direction (wdir). Grey circles
 466 indicate measurements collected between 26 January and 1 February 2014 at JFJ station, while
 467 modeled values from CNTRL simulation are shown with a black line. The semi-transparent
 468 contour plot is representing the vertical velocity (w) profile predicted by the CNTRL
 469 simulation. Each day starts at 00:00 UTC.
 470

471
 472 Throughout the two case studies, the WRF simulations seem to closely follow the
 473 observed temperatures (Fig. 2a), which is also indicated by the high IoA in Table 1. The

474 synoptic situation occurring on 26 January, with a deep trough extending to western Europe
 475 (Fig. 1), has been associated with intense snowfalls in the alpine regions (Panziera and Hoskins,
 476 2008). The passage of the cold front was followed by a sharp temperature decrease, with the
 477 simulated temperatures fluctuating between -10 and ~ -20 °C throughout the NW case (Fig.
 478 2a). Under the influence of the warm front during the SE case, the modeled temperatures rose
 479 from ~ -18 °C to ~ -14 °C and remained less variable until 30 January 12:00 UTC, with mean
 480 values of ~ -15.5 °C (Table 1).

481

482 **Table 1.** Mean modeled values (\pm standard deviations), RMSE and IoA between the CNTRL
 483 simulation of WRF and measurements carried out by the MeteoSwiss station at JFJ.

Variable	Mean \pm std		RMSE		IoA	
	NW winds	SE winds	NW winds	SE winds	NW winds	SE winds
T2m (°C)	-17.10 ± 4.36	-15.48 ± 1.75	1.40	1.33	0.97	0.84
RH2m (%)	94.07 ± 7.02	94.24 ± 10.31	14.01	11.61	0.55	0.64
wspd (ms^{-1})	15.57 ± 7.45	9.78 ± 3.94	4.85	6.75	0.88	0.22

484

485 Fig. 2c and 2d reveal that the 1-km resolution domain can sufficiently capture the local
 486 wind systems to a certain extent. During the NW flow, the horizontal wind speeds are
 487 reproduced better by the CNTRL simulation (IoA=88%), whereas during the SE winds, the
 488 simulated wind speed is frequently underestimated compared with observations (Fig. 2c). Such
 489 deviations in the horizontal wind speed might be caused by the relatively coarse horizontal
 490 resolution of the model, which prevents some small-scale and very local orographic structures
 491 from being resolved. As discussed in Section 2.2, the observed winds at JFJ are channeled by
 492 the orography to either NW or SE directions. The CNTRL simulation of WRF can satisfactorily
 493 reproduce the wind direction in both cases, although the simulated values exhibit larger
 494 fluctuations than the measured ones (Fig. 2d), presumably because of the surrounding
 495 orography being less accurately represented in the model. This is particularly evident during
 496 NW winds, when the simulated wind directions shift slightly to west directions compared to
 497 observations. The positive vertical velocities, illustrated in the contour plot in Fig. 2d, result
 498 from the orographically forced lifting of the airmasses over the local topography, and are not
 499 related to convective instability in the lower atmospheric levels. The stronger updrafts
 500 prevailing until the end of 26 January are associated with the steep ascent of the air parcels,

501 which can also contribute to the enhanced relative humidity (Fig. 2b). After the frontal passage,
502 the vertical velocities at the lower levels are downward directed, with the vertical profile of
503 potential temperature revealing that the atmosphere at JFJ is stabilized (not shown). The same
504 vertical velocity pattern, with mainly downward motions, characterizes the stably stratified
505 atmosphere after 30 January. Overall, Fig. 2 suggests that local meteorological conditions at
506 JFJ are reasonably well represented by the model.

507

508 2.4 Model simulations

509 Given the good representation of the atmospheric conditions at JFJ, the CNTRL simulation of
510 WRF is further accompanied by ~~four~~five sensitivity simulations, aiming to investigate the
511 contribution of BR and DS mechanisms. Here we also perform three additional sensitivity
512 experiments to explore the potential impact of blowing ice and the synergistic interaction with
513 SIP on the development of the simulated MPCs. A detailed list of the sensitivity experiments
514 is provided in Table 2.

515 The contribution of the DS mechanism is addressed in two sensitivity experiments,
516 DS_PHILL and DS_SULL, where the parameterizations of Phillips et al. (2018) and Sullivan
517 et al. (2018a) were applied, respectively (Section 2.2.4). Both sensitivity simulations yield
518 predictions that coincide with the CNTRL simulation (supplement Fig. S1) suggesting that the
519 DS mechanism is hardly ever activated, and fail to produce realistic total ice number
520 concentrations (N_{isg} ; cloud ice + snow + graupel). The absence of correlation between LWC
521 and N_{isg} fluctuations might also suggest the ineffectiveness of this mechanism under the
522 examined conditions. Note that the parameterized expressions used to describe the DS
523 mechanism involve a number of empirical and rather uncertain parameters, the value of which
524 could potentially influence the efficiency of the process in producing secondary ice fragments.
525 However, the sensitivity of our results to the choice of these parameters would be negligible,
526 as the low concentrations ($\lesssim 10^2 \text{ cm}^{-3}$) of relatively small raindrops with mode diameters
527 below the threshold size of 50 μm seem to completely prevent the onset of the DS process
528 (supplement Fig. S2). The DS mechanism is therefore excluded from the following discussion.
529 This result is in line with the modeling study of Dedekind et al. (2021), who also
530 ~~highlighted~~reported the inefficiency of this mechanism in wintertime alpine clouds.

531 ~~Two additional~~Three sensitivity simulations are also conducted ~~to investigate if activating~~
532 the ~~BR mechanism can account for the observed ICNCs.~~generation of secondarily formed ice
533 particles through BR. First, the TAKAH simulation, adopts the temperature-dependent formula

Formatted: Superscript

Formatted: Superscript

534 of Takahashi et al. (1995) scaled with the size of ~~the~~ particles that undergo fragmentation
535 (Sotiropoulou et al. 2021a) ~~is tested in the TAKAH simulation. The PHILL simulation is then~~
536 ~~conducted to test the performance of the more advanced Phillips et al. (2017a)~~
537 ~~parameterization. Note that the parameters involved in the parameterized expression of N_{BR}~~
538 ~~(Eq. 3) concern the effect of ice habit and rimed fraction of the colliding). Applying Equation~~
539 ~~(2) to collisions between all ice particles—which is not explicitly resolved—categories considered~~
540 in the M05 scheme. ~~Regarding the ice habit, we assume spatial planar—(except collisions~~
541 ~~between cloud-ice particles, based on the imagery presented in Lloyd et al. (2015) and; Section~~
542 ~~2.2.3) inserts Cuzzioli et al. (2015), which revealed the predominance of sectored plates and~~
543 ~~oblate particles (probably columns or needles), along with some rimed hydrometeors, at~~
544 ~~temperatures —15 °C. Balloon borne measurements taken in low level orographic MPCs~~
545 ~~within seeder feeder events revealed the presence of a large fraction of graupel and rimed~~
546 ~~particles (Ramelli et al., 2021). For this reason, during the NW and SE cases we consider rimed~~
547 ~~fractions of 0.4 and 0.3 to account for heavily and moderately rimed ice particles, respectively.~~
548 ~~A higher rimed fraction is prescribed for the NW winds case study though, as the co-existence~~
549 ~~of ice crystals and liquid droplets under the stronger updraft conditions are expected to~~
550 ~~favor~~ caveat to our approach. The laboratory results of Takahashi et al. (1995) suggest that, it
551 is mostly the collisions between rimed particles and graupel that are more conducive to SIP
552 through BR. Vardiman (1978) also reported that ice crystal growth through riming. ~~However,~~
553 ~~the~~ is essential to boost fragmentation. Applying the Takahashi break-up scheme for unrimed
554 ice particles might, therefore, overestimate the number of secondary ice fragments. To test this
555 hypothesis, we performed TAKAHrim sensitivity of our results to the rimed fraction was not
556 found significant simulation, where we enabled ice multiplication through BR only after
557 collisions between rimed cloud ice/ snow and graupel particles. To diagnose the presence of
558 rime on ice particles we used the amount of cloud droplets or raindrops accreted by snow and
559 cloud ice, which is predicted in the M05 scheme.

560

561

Table 2. List of sensitivity simulations conducted with ~~the~~ WRF model.

Simulation	BR process	DS process	NBIPS (L ⁻¹)
CNTRL	off	off	0
DS_PHILL	off	Phillips et al., 2018	0
DS_SULL	off	Sullivan et al., 2018a	0
TAKAH	Takahashi et al., 1995	off	0

Formatted: Indent: First line: 0 cm

Formatted Table

Formatted: Space After: 6 pt

Formatted: Space After: 6 pt

Formatted: Space After: 6 pt

Formatted: Space After: 6 pt

<u>TAKAHrim</u>	<u>Takahashi et al., 1995</u> <u>activated only after</u> <u>collisions between rimed</u> <u>ice particles</u>	<u>off</u>	<u>0</u>
PHILL	Phillips et al., 2017a	off	0
BIPS10	off	off	10
BIPS100	off	off	100
BIPS100_ PHILL	Phillips et al., 2017a	off	100

Formatted: Space After: 6 pt

Formatted Table

Formatted: Space After: 6 pt

Formatted: Space After: 6 pt

562

563 Finally, the performance of the more advanced Phillips et al. (2017a) parameterization is
564 tested in the PHILL simulation. Parameters involved in the Phillips parameterization that are
565 not explicitly resolved in the M05 microphysics scheme are the rimed fraction and the ice habit
566 of colliding ice particles. The choice of ice habit is based on particle images collected during
567 the CLACE 2014 campaign, showing the presence of non-dendritic sectored plates and oblate
568 particles at temperatures ~ -15 °C (Lloyd et al., 2015). Grazioli et al. (2015) also presented
569 some examples of particle imagery produced by a 2D-S imaging probe, revealing the presence
570 of heavily rimed hydrometeors, as well as highly oblate particles (probably columns or
571 needles). The rimed fraction, is prescribed to a value of 0.4 (0.3) to account, respectively, for
572 heavily and moderately rimed ice particles present under NW (SE) wind conditions. A high
573 degree of riming is expected in the simulated cases, as they both occur under ice-seeding
574 situations (Section 3.1.1), where large precipitating ice particles from the seeder clouds
575 effectively gain mass in the mixed-phase zone through riming. Direct observations with
576 balloon-borne measurements carried out within ice-seeding events in the region around Davos
577 in the Swiss Alps support the presence of a large fraction of rimed particles and graupel
578 (Ramelli et al., 2021). The higher riming degree is prescribed under NW-winds because the
579 orographic forcing (i.e., vertical velocity) is stronger and helps maintaining mixed-phase
580 conditions in the feeder clouds – which in turn promotes ice crystal growth through riming.
581 However, our results were not very sensitive to the choice of the rimed fraction.

582 The remaining sensitivity simulations focus on the potential impact of BIPS. A recently-
583 developed blowing snow scheme, used to simulate alpine snowpacks, reported significant mass
584 and number mixing ratios of BIPS that can be found up to ~1 km above the surface under high
585 wind speed conditions (see Fig. 17 in Sharma et al., 2021) with the potential to trigger cloud
586 microphysical processes. Given that in the default M05 scheme there is no parameterization of
587 a flux of ice particles from the surface, we parameterize the effect of BIPS lofting into the
588 simulated orographic clouds by applying a constant ice crystal source to the first atmospheric

589 level of WRF over the whole model domain. Although the source of BIPS at the first model
590 level remained constant, yet their number will be affected by processes such as advection,
591 sublimation and sedimentation, that are described in the M05 scheme. Note that the relatively
592 coarse horizontal resolution in the innermost domain of our simulations (i.e., 1 km) does not
593 allow the accurate representation of the small-scale turbulent flow over the orographic terrain.
594 This is considered a limitation of our methodology, since turbulent diffusion is a key process
595 affecting the amount of BIPS that will be resuspended from the surface.

596 The applied concentrations of BIPS varied between 10^{-2} and 100 L^{-1} , which is the upper
597 limit proposed by Lloyd et al. (2015) and observed within in-cloud conditions by Beck et al.
598 (2018). Number concentrations of BIPS (i.e., NBIPS) lower than 10 L^{-1} were found incapable
599 of affecting the simulated cloud properties and are, therefore, not included in the following
600 discussion. Two sensitivity simulations are finally performed, BIPS10 and BIPS100 (Table 2),
601 in which the number indicates the NBIPS in L^{-1} . In our approach we assume BIPS are spherical
602 with diameters of $100 \mu\text{m}$, based on typical sizes that are frequently reported in the literature
603 (e.g., Schlenczek et al., 2014; Schmidt, 1984; Geerts et al., 2015; Sharma et al., 2021). The
604 relatively small fall speed of these particles (e.g., Pruppacher and Klett, 1997) will allow them
605 to remain suspended in the atmosphere. As a sensitivity we also considered smaller particles
606 with sizes of $10 \mu\text{m}$, but our results did not change significantly (supplement Fig. S3).
607 ~~Besides~~ Nevertheless, such small ice particles are not expected to substantially contribute to the
608 simulated IWC, as shown by Farrington et al. (2016).

609 As SIP through BR and blowing snow are both important when trying to explain the high
610 ICNCs observed in alpine environments, their combined effect is addressed in our last
611 simulation, BIPS100_PHILL (Table 2). In this sensitivity simulation the effect of BR is
612 parameterized after Phillips et al. (2017a), while a constant ice crystal concentration of 100 L^{-1}
613 is applied to the first atmospheric level of WRF to represent the effect of BIPS.

614

615 3. Results and discussion

616

617 3.1 Impact of SIP through BR on simulated microphysical properties

618 ~~Fig. 3 displays the~~ The temporal evolution of ~~the~~ N_{isg} , IWC and LWC, at the first model level
619 ($\sim 10 \text{ m a.g.l.}$) from the nearest to JFJ model grid point of the CNTRL, TAKAH and PHILL
620 simulations. ~~Note that instead is presented in Fig. 3. Instead~~ of focusing on a single grid point,
621 we also averaged the results from the 9-km^2 area surrounding the point of interest. However,

Formatted: English (United States)

Formatted: English (United States)

Field Code Changed

Formatted: English (United States)

Formatted: Font color: Auto

622 the produced time series showed only little difference when compared to the nearest grid point
623 time series, ~~further validating the robustness of our results~~ (not shown), ~~ensuring our analysis~~
624 ~~is robust~~. Besides, the region in the vicinity of JFJ is very heterogeneous supporting the single
625 point comparison presented in the following discussion. The grey dots shown in Fig. 3
626 represent the measurements taken by the 2D-S and CDP instruments at JFJ throughout the two
627 periods of interest. The displayed time frequency of the observations is 30 min to match the
628 output frequency of the model. Note that the simulated LWC includes liquid water from cloud
629 droplets and rain, while the simulated IWC includes cloud ice, snow and graupel. The
630 contribution of rain in our simulations is, however, negligible (supplement Fig. S2). Several
631 statistical metrics for N_{isg} , IWC and LWC are summarized in Table 3, 4 and 5, respectively.
632 ~~Note that periods~~ Periods with missing data in the measurement time series are excluded from
633 the statistical analysis.

634 During the NW flow, between 26 and 28 January, the measured ICNCs exceed 100 L^{-1}
635 for >50 % of the time, whereas during the SE flow the ICNCs usually fluctuate between 10 and
636 100 L^{-1} (Fig. 3a). The highest ICNCs are generally observed at temperatures higher than ~ -15
637 $^{\circ}\text{C}$, where SIP processes are thought to be dominant and primary ice nucleation in the absence
638 of bioaerosols is limited (e.g., Hoose and Möhler, 2012; Kanji et al., 2017). The CNTRL
639 simulation fails to reproduce N_{isg} higher than 10 L^{-1} , with the mean simulated values being ~ 2 -
640 2.5 L^{-1} during both periods. At the same time the mean observed ICNC values are ~ 200 (70)
641 L^{-1} during the NW (SE) case. Thus, CNTRL systematically underestimates the amount of ice
642 by up to 2 orders of magnitude, which is also consistent with the interquartile statistics
643 presented in Table 3. With the HM process being totally ineffective in the prevailing
644 temperatures, this discrepancy suggests that ice crystals produced by heterogeneous ice
645 nucleation in CNTRL are not high enough to match the observations. A similar discrepancy
646 between predicted INPs and measured ICNCs was also documented in Lloyd et al. (2015).

647

648 **Table 3.** The 25th, 50th (median) and 75th percentiles of ICNC time series (in L^{-1}).

Simulation	25 th perc.		Median		75 th perc.	
	NW winds	SE winds	NW winds	SE winds	NW winds	SE winds
OBSERVED	8.69	6.64	80.47	34.53	261.25	88.69
CNTRL	0.76	0.84	2.02 1.68	2.02 1.68	2.80	3.60
TAKAH	2.27	1.08	9.85	122.56	362.51	358.38
<u>TAKAHrim</u>	<u>2.56</u>	<u>0.75</u>	<u>12.30</u>	<u>4.17</u>	<u>101.46</u>	<u>82.16</u>

PHILL	2.49	0.76	6.27	2.09	118.21	59.23
BIPS10	1.60	1.90	2.42	2.72	3.30	4.78
BIPS100	6.17	10.74	10.36	13.88	12.32	17.39
BIPS100_PHILL	8.95	11.51	15.87	16.30	138.92	98.43

649
650 Activating the BR process in TAKAH, TAKAHrim and PHILL simulations is found to
651 produce N_{isg} as high as 400 L^{-1} during both case studies (Fig. 3a), resulting in a substantially
652 better agreement with observations. At times when the simulated temperatures drop below $\sim -$
653 $18 \text{ }^\circ\text{C}$, the N_{isg} modeled by ~~both~~ all three simulations coincide with the CNTRL simulation. At
654 relatively warmer subzero temperatures though, the significant contribution of the BR process
655 is evident, elevating the predicted N_{isg} by up to 3 orders of magnitude during the NW case and
656 by more than 2 orders of magnitude during the SE case. Although the median N_{isg} in TAKAH
657 and PHILL all three sensitivity simulations with active break-up remains underestimated
658 compared to observations during the NW flow, ~~the first~~ TAKAH seems to produce
659 unrealistically high median and 75th percentile values during the SE flow (Table 3). Indeed,
660 focusing on the N_{isg} time series (Fig. 3a) TAKAH is $\sim 25\%$ of the time shown to overestimate
661 the observed ICNCs by a factor of ~ 3 , reaching up a factor of 10 on 30 January at 00:00.
662 TAKAHrim and PHILL, on the other hand, ~~produces~~ produce more reasonable N_{isg}
663 concentrations of ice particles throughout both case studies, ~~increasing with the~~ N_{isg} values in
664 the 75th percentile ~~by more than~~ exceeding $100 (50) \text{ L}^{-1}$ during the NW (SE) case study (Table
665 3), ~~reducing which is found to reduce~~ the gap between observations and model predictions.

666 It is worth noting that, despite the fact that the Takahashi parameterization (Eq. 2) is
667 applied to both TAKAH and TAKAHrim simulations, the former seems to systematically
668 overestimate the number of secondary ice fragments, while the latter produces ICNCs that are
669 more consistent with the observations. Hence the Takahashi parameterization predicts
670 reasonable results if it is allowed to generate fragments from collisions between rimed ice
671 particles only (Section 2.4).

672
673 **Table 4.** The 25th, 50th (median) and 75th percentiles of IWC (in gm^{-3}) time series.

Simulation	25 th perc.		Median		75 th perc.	
	NW winds	SE winds	NW winds	SE winds	NW winds	SE winds
OBSERVED	31.5×10^{-3} <u>0.03</u>	22.0×10^{-3} <u>0.02</u>	0.63 <u>19</u>	0.24 <u>11</u>	0.66	0.26
CNTRL	4.3×10^{-3}	5.0×10^{-3}	0.03	0.04	0.15	0.12

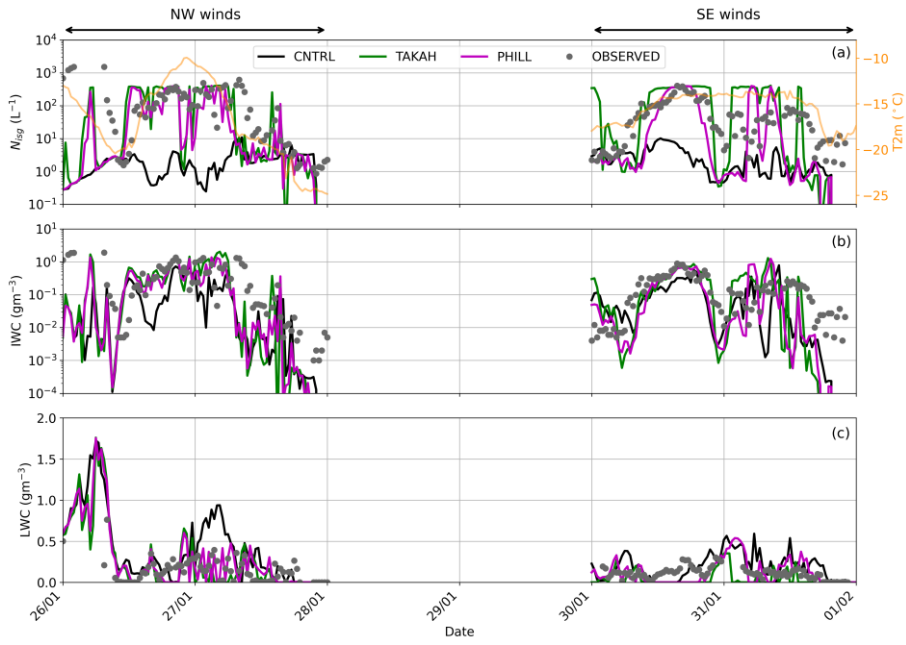
TAKAH	1.3×10^{-3}	2.0×10^{-3}	0.10	0.09	0.52	0.34
<u>TAKAHrim</u>	<u>4.7×10^{-3}</u>	<u>3.1×10^{-3}</u>	<u>0.08</u>	<u>0.04</u>	<u>0.33</u>	<u>0.27</u>
PHILL	3.8×10^{-3}	3.7×10^{-3}	0.10	0.02	0.38	0.30
<u>BIPS100_PHILL</u>	<u>3.9×10^{-3}</u>	<u>9.01×10^{-3}</u>	<u>0.09</u>	<u>0.03</u>	<u>0.40</u>	<u>0.3+30</u>

674
675 The observed IWC time series (Fig. 3b) are frequently reaching $\sim 1 \text{ gm}^{-3}$ during the NW
676 case, with the median values being a factor of 2.5 higher than those observed during the SE
677 case (Table 4). This ~~highlights~~indicates the presence of more massive ice particles when higher
678 updraft velocities prevail. The CNTRL simulation cannot produce IWC values $> 0.8 \text{ gm}^{-3}$ and
679 is most of the time below the observed range. Adding a description of the BR process (i.e., in
680 TAKAH, TAKAHrim and PHILL ~~simulations~~) sufficiently increases the modeled IWC by up
681 to ~ 1 order of magnitude between 26 January 12:00 UTC and 27 January 06:00 UTC, when
682 the modeled N_{isg} exceeds 100 L^{-1} and the ~~temperatures remain~~temperature remains higher than
683 $-16 \text{ }^\circ\text{C}$. The same conditions are observed in the SE case, between 12:00 and 18:00 UTC on
684 30 January, when IWC shows a ~ 3 fold enhancement reaching the observed levels. The IWC
685 values in the third quartile predicted by TAKAH, TAKAHrim and PHILL are more than a
686 factor of 2 higher than the ones predicted by CNTRL (Table 4). This increase improves the
687 model performance although the modeled IWC remains slightly underestimated
688 (overestimated) during the NW (SE) case. The size distribution of the three ice ~~hydrometeors~~
689 ~~assumed by all three sensitivity simulations~~species considered in the M05 scheme (supplement
690 Fig. S4) reveals that, the implementation of the BR mechanism ~~produces~~leads to elevated
691 concentrations of relatively smaller cloud ice crystals, but at the same time increases the
692 concentrations of snow particles. This is the reason why the modeled total ice mass is also
693 increased compared with the CNTRL simulation.

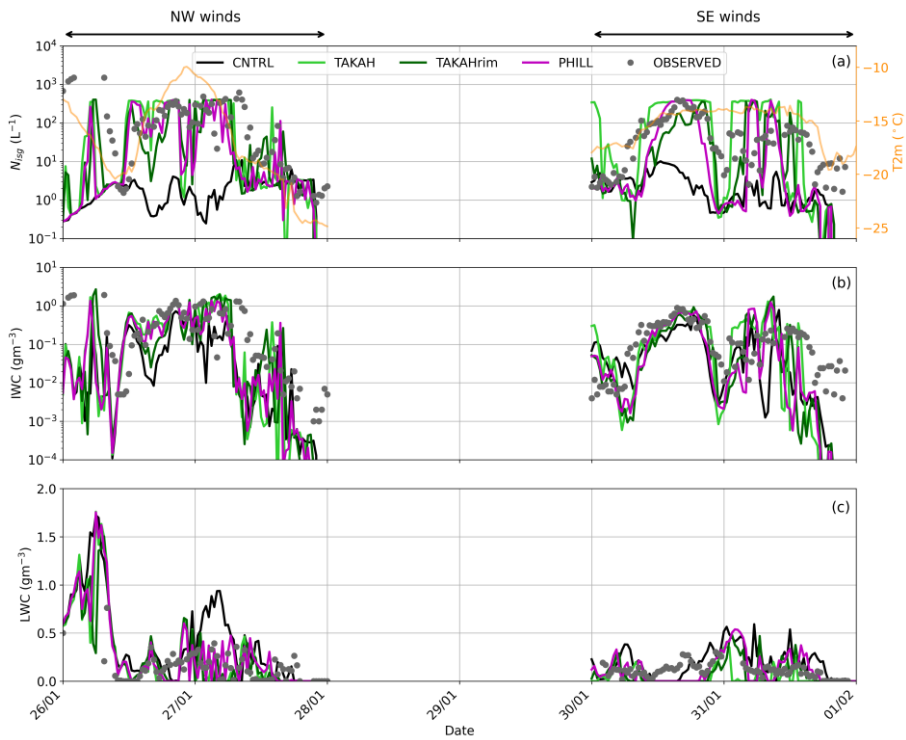
694 Fig. 3c compares the simulated cloud LWC to the concurrent CDP observations at JFJ
695 ~~station~~. The LWC values recorded during the NW case are highly variant, reaching up to 0.75
696 gm^{-3} , which is substantially higher than the respective maximum LWC observed during the SE
697 case (0.30 gm^{-3}). On 26 January before 12:00 UTC, all ~~three~~-sensitivity simulations predict
698 $\text{LWC} > 1 \text{ gm}^{-3}$, which, however, cannot be validated against measurements due to missing
699 ~~values~~data in the CDP time series. Note that this period is excluded from the statistics derived
700 in Table 5. The CNTRL simulation is found to overestimate the cloud LWC, predicting 0.42
701 (0.25 gm^{-3}) in the third quartile, which is a factor of ~ 2 higher than the ~~mean LWC~~-observed
702 values during the NW (SE) case (Table 5).

Formatted: Indent: First line: 1 cm, Line spacing: 1,5 lines, Don't keep with next

704



705



706 **Figure 3.** Time series of (a) total N_{isg} and temperature at 2 m height (orange line), (b) IWC and
 707 (c) LWC, predicted by the CNTRL (black line), TAKAH (light green line), TAKAHrim (dark
 708 green) and PHILL (magenta line) simulations between 26 January and 1 February 2014. The
 709 grey dots in all three panels represent the 2D-S ICNCs, the inferred IWC and the CDP LWC
 710 measured at the JFJ station, respectively. Note the logarithmic y-axes in panels a and b.

711
 712 The modeled LWC in the 75th percentile is decreased by a factor of ~~>2.5~~ (~~→1.5~~) ~~5~~ in
 713 ~~TAKAH (PHILL)~~ the simulations that account for the BR process (Table 5), improving the
 714 agreement with observations (Fig. 3c). ~~This~~The reduction in LWC is expected, considering that
 715 the higher N_{isg} produced when BR is activated can readily deplete the surrounding droplets
 716 under liquid water subsaturated conditions through the WBF process. This introduces a
 717 challenging environment to simulate, as the model is sometimes seen to convert water to ice
 718 too rapidly, leading to cloud glaciation (e.g., on 30 January after 12:00 UTC). Despite all sinks
 719 of cloud water (i.e., condensation freezing, WBF or riming), observations at JFJ suggest that
 720 mixed-phase regions are generally sustained (Lloyd et al., 2015). This is particularly true for
 721 the NW case, when the sufficiently large updrafts caused by the steep ascent of the air masses
 722 help maintain the supersaturation with respect to liquid water (Lohmann et al., 2016). PHILL
 723 and TAKAHrim can more efficiently sustain the observed mixed-phase conditions compared
 724 to TAKAH, which frequently results in explosive ice multiplication – especially during the SE
 725 case – leading to an underestimation of the LWC (see Fig. ~~3e and Table 5~~); 3c and Table 5).
 726 TAKAH is, therefore, excluded from the following discussion as it fails to reproduce an
 727 accurate liquid and ice partitioning.
 728

729 **Table 5.** The 25th, 50th (median) and 75th percentiles of LWC (in gm^{-3}) time series.

Simulation	25 th perc.		Median		75 th perc.	
	NW winds	SE winds	NW winds	SE winds	NW winds	SE winds
OBSERVED	8.5×10^{-3}	70.0×10^{-3}	0.12	0.11	0.21	0.14
CNTRL	87.7×10^{-3}	26.0×10^{-3}	0.19	0.17	0.42	0.25
TAKAH	1.3×10^{-10}	0.0	0.01	6.7×10^{-10}	0.16	0.05
<u>TAKAHrim</u>	<u>1.2×10^{-7}</u>	<u>0.0</u>	<u>0.06</u>	<u>2.8×10^{-6}</u>	<u>0.23</u>	<u>0.09</u>
PHILL	6.3×10^{-8}	0.0	0.09	0.03	0.26	0.18
BIPS10	82.0×10^{-3}	4.6×10^{-3}	0.18	0.12	0.33	0.24
BIPS100	67.1×10^{-3}	13.1×10^{-3}	0.18	0.13	0.36	0.23
BIPS100_PHILL	6.3×10^{-10}	0.0	0.09	0.06	0.27	0.10

730

Formatted: Indent: First line: 1 cm

Formatted: Font color: Auto

731 The time-averaged vertical profiles of ~~number concentrations of~~ cloud ice (N_i), graupel
732 (N_g), snow (N_s) and total N_{ice} number concentrations are illustrated in Fig. 4 for the CNTRL,
733 ~~TAKAH~~TAKAHrim and PHILL simulations. The mean N_i (Fig. 4a) and N_{ice} profiles (Fig. 4d)
734 are enhanced by more than up to 2 orders of magnitude enhanced in TAKAHrim and
735 PHILL compared to CNTRL. It is again obvious that TAKAH produces higher concentrations
736 than PHILL, at least~~During the NW flow both simulations including the BR process produce~~
737 similar vertical distribution of the ice hydrometeors in the lower 2 (lowest 1) 1.5 km of in the
738 atmosphere. This is not the case for the SE case, where TAKAHrim seems to predict a rapid
739 decrease in N_i and N_s and thus in total N_{ice} with altitude. The main difference between these
740 two simulations lies in the fact that the total LWC and hence, the probability of riming,
741 decreases with height limiting the efficiency of BR in TAKAHrim. This become more evident
742 during the NW (SE) case. As discussed above, this regularly leads to overestimated N_{ice}
743 compared with the observed amount of ice close to the surface. All three simulations, however,
744 produce similar results~~SE case where mixed-phase conditions are exclusively confined below~~
745 1.5 km in the atmosphere (Section 3.1.1). However, we cannot estimate which vertical
746 distribution better represents reality, due to the lack of corresponding measured profiles.
747 TAKAHrim coincides with PHILL only when there is sufficient liquid water in the atmosphere,
748 allowing for the riming of the ice hydrometeors. Moreover, at heights above ~2.5 km, where
749 the simulated temperatures drop well below -20 °C (supplement Fig. S5-S5), all three
750 simulations are seen to produce similar results. This implies the greater importance of SIP
751 through BR at heights below 2-3 km in the atmosphere (i.e., in the temperature range between
752 ~ -18 °C and ~ -10 °C).

753

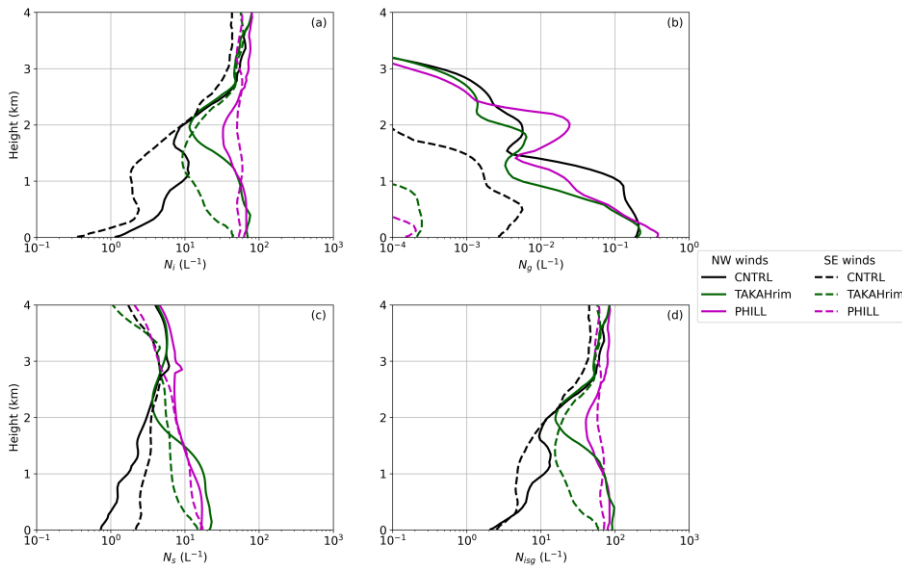
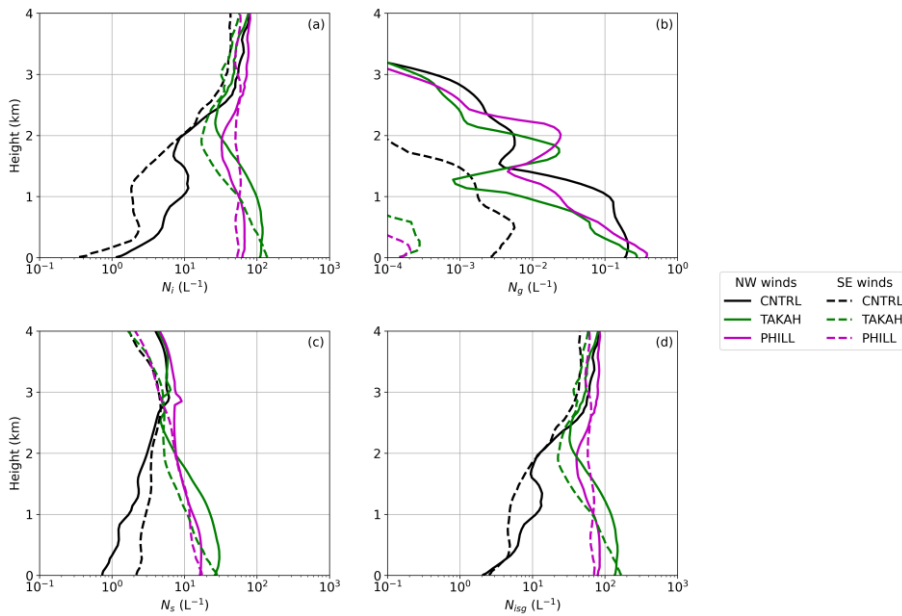


Figure 4. Mean vertical profiles of (a) N_i , (b) N_g , (c) N_s and (d) total N_{isp} , predicted by the CNTRL (black), TAKAHrim (dark green) and PHILL (magenta) simulations for the NW (solid lines) and SE (dashed lines) cases. Note the different scale on the x axis of the N_g vertical distribution. The height is given in km a.g.l.

Graupel number concentrations (Fig. 4b) do not contribute much to the modeled ice phase, especially during the SE case when the simulated N_g is negligible compared with the N_i and N_s (Fig. 4c). In the M05 scheme, portion of the rimed cloud or rain water onto snow is allowed to convert into graupel (Reisner et al. 1998), provided that snow, cloud liquid and rain water mixing ratios exceed a threshold of 0.1, 0.5 and 0.1 g kg^{-1} , respectively. These mixing ratio thresholds for graupel formation are arbitrary and might not be suitable for the examined conditions, preventing the formation of graupel from rimed snowflakes (Morrison and Grabowski, 2008). During the NW case, however, we can identify substantially higher N_g than the SE case, owing to the presence of sufficient supercooled liquid water especially during the first half of 26 January. Activating the BR mechanism in ~~TAKAH~~TAKAHrim and PHILL generally decreases the simulated N_g in both cases (Fig. 4c), suggesting that break-up of graupel contributes to ice multiplication.

Formatted: Indent: First line: 0 cm



773
 774 **Figure 4.** Mean vertical profiles of (a) N_i , (b) N_g , (c) N_s and (d) total N_{tot} , predicted by the
 775 CNTRL (black), TAKAH (green) and PHILL (magenta) simulations for the NW (solid lines)
 776 and SE (dashed lines) cases. Note the different scale on the x axis of the N_g vertical distribution.
 777 The height is given in km a.g.l.

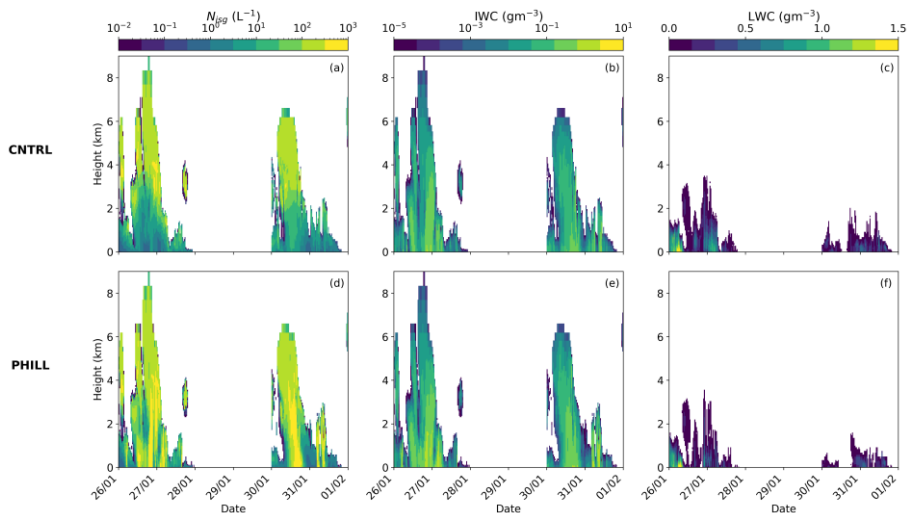
778
 779 The mean vertical profile of N_s (Fig. 4c) seems to follow the respective profile of N_i (Fig.
 780 4a). Unlike the graupel concentrations, including the BR mechanism is found to enhance N_s up
 781 to one order of magnitude compared to the CNTRL simulation. Focusing on a single model
 782 time step when the BR mechanism is activated, the size distribution of snow particles shown
 783 in the supplement Fig. S4 reveals that the increase in snow number concentrations can reach
 784 up to 2 orders of magnitude during the NW case. This is a logical consequence of the increase
 785 in number concentration of ice crystals, which are converting to snow particles after ice crystal
 786 growth (i.e., cloud-ice-to-snow autoconversion), when surpassing a characteristic mean
 787 diameter of 250 μm . This will be discussed in detail in the following section, which is focused
 788 We focus subsequent discussion on the PHILL simulation as it because i) TAKAHrim provides
 789 a slightly more accurate representation comparable results in terms of the in-cloud phase
 790 partitioning compared with TAKAH, and, ii) we explore the sensitivity of simulation results to
 791 parameters not considered by the Takahashi formulation.

Formatted: Indent: First line: 0 cm

793 *3.1.1 Conditions favoring BR in the two considered events*

794 The temporal evolution of the vertical profiles of N_{isg} , IWC and LWC can provide valuable
795 insight on the drivers of enhanced ice formation in the wintertime alpine MPCs. Fig. 5 reveals
796 the presence of a seeder-feeder cloud system with sustained mixed-phase conditions confined
797 to levels below ~ 3 km (~ 1.5 km) in the NW (SE) case and a pure ice cloud aloft. Such
798 configurations are a well-known type of orographic multi-layer clouds that enhances
799 precipitation over mountains (e.g., Browning et al., 1974, 1975; Roe, 2005). Cloud
800 condensation is promoted by the synergy between a midlatitude frontal system and its
801 orographically induced ascent over the mountain range (Fig. 1). The separation between the
802 seeder and feeder clouds is often nonexistent, meaning that ice seeding can occur either in
803 layered clouds or internally within one cloud (Roe, 2005; Proske et al., 2021). In the first case,
804 which seems to occur here as well, there can be vertical continuum of cloud condensates
805 between the seeder and the feeder cloud due to precipitation of ice crystals from the higher-
806 level cloud (Fig. 5a). This means that the seeding ice crystals fall through subsaturated cloud-
807 free air before reaching the feeder region of the cloud and might sublime. ~~A~~The remote-
808 sensing analysis ~~to 11 year of data~~ over Switzerland presented by Proske et al. (2021), showed
809 that in-cloud seeding occurs in 18% of the observations, while the external seeder-feeder
810 mechanism is present 15% of the time ~~(Proske et al., 2021) when the seeder is a cirrus~~
811 ~~cloud~~ when the seeder is a cirrus cloud.

812

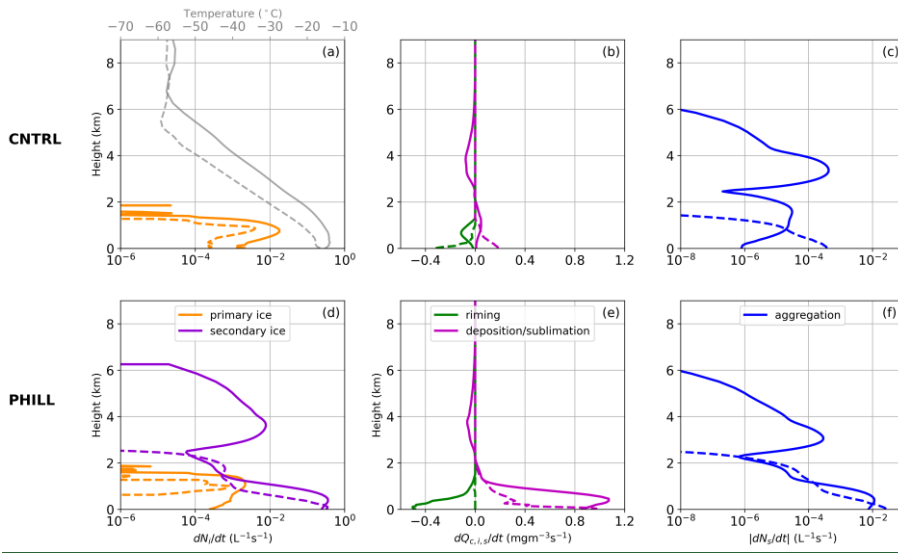


813 **Figure 5.** Time-height plots of total N_{isg} (a, d), IWC (b, e) and LWC (c, f) produced by CNTRL
 814 (top panel) and PHILL (bottom panel) simulations between 26 January and 1 February 2014.
 815 The height is given in km a.g.l.
 816

817
 818 To illustrate the processes taking place during the two cases of interest, Fig. 6 displays
 819 the tendency of primary and secondary ice production as well as the growth of ice particles
 820 through deposition, riming and aggregation from the CNTRL and PHILL simulations at 17:00
 821 (19:00) UTC on 26 (30) January. The vertical profiles on 26 January are taken within the
 822 seeder-feeder event, while those on 30 January are taken when the high-level cloud associated
 823 with the warm front has already passed the region of interest. Upon arrival of the frontal system
 824 on 26 January, ~~the CNTRL simulation~~ indicates a rapid increase of the total N_{isg} near cloud top
 825 (Fig. 5a), which is not shown in the vertical profile of ~~the~~ primary ice production rates taken at
 826 17:00 UTC (Fig. 6a). The ice particles consisting the seeder cloud are, therefore, formed far
 827 from the JFJ station and seem to be advected over the domain of interest. Primary ice crystals
 828 are formed in both cases below 2 km in the feeder cloud at temperatures lower than -30 °C
 829 through heterogeneous freezing (Fig. 6a). At these heights supercooled liquid water is also
 830 present (Fig. 5c) and the newly formed ice particles start growing initially by vapor deposition
 831 due to supersaturation with respect to ice, followed by riming (Fig. 6b). This is also indicated
 832 by the increased IWC values closer to the ground (Fig. 5b).
 833

Formatted: Font color: Auto

Formatted: Indent: First line: 0 cm

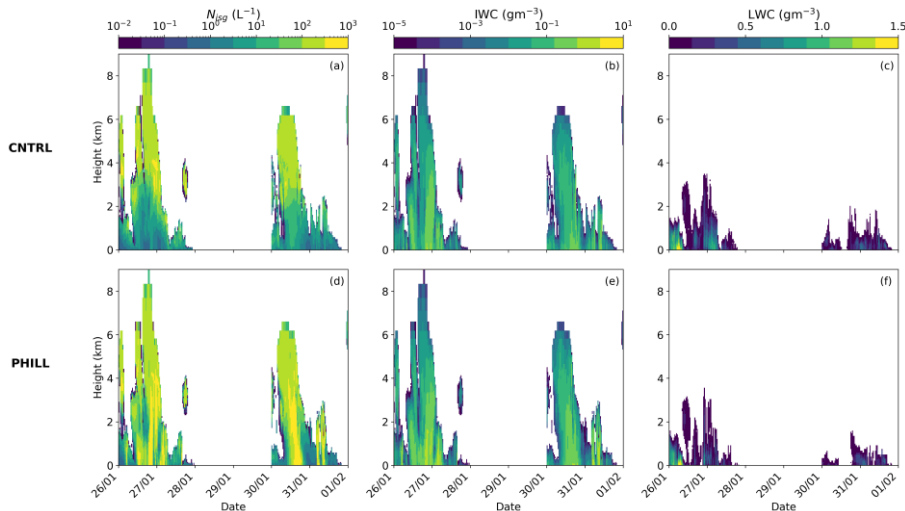


834

835 **Figure 6.** Vertical profiles of (a, d) primary and secondary ice production, (b, e) riming and
 836 vapor deposition or sublimation and (c, f) snow aggregation produced by the CNTRL (top
 837 panel) and PHILL (bottom panel) simulations at 17:00 UTC on 26 January (solid line) and at
 838 19:00 UTC on 30 January (dashed line). The vertical profile of simulated temperature is also
 839 superimposed in (a). The cloud liquid water content (Q_c) is shown in panels (b and e) to
 840 represent the tendency due to riming, while the mass mixing ratio of the ice and snow species
 841 ($Q_i + Q_s$), are representing the relative tendencies due to vapor deposition or sublimation. Note
 842 that the tendencies due to snow aggregation in (c, f) are presented in absolute values. The height
 843 is given in km a.g.l.

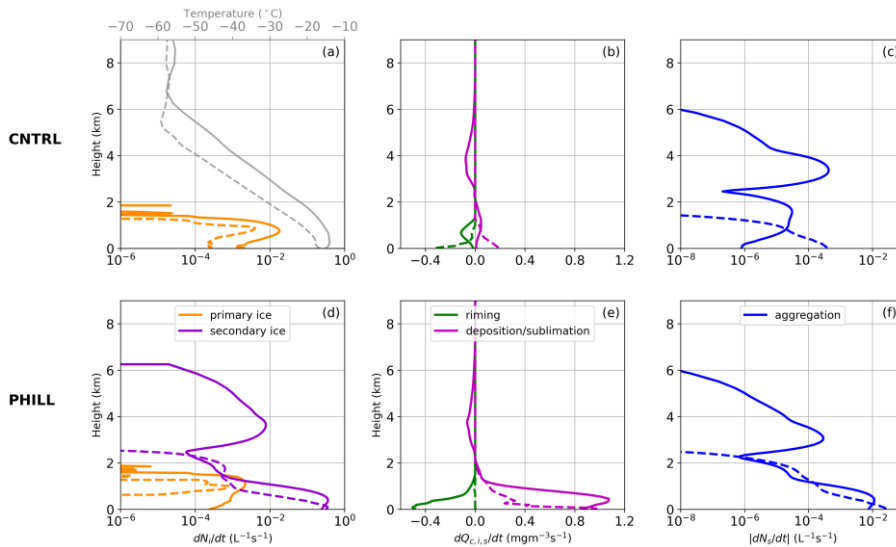
844

Formatted: Font: 12 pt, Not Italic, Font color: Text 1



845 ~~Figure 5. Time-height plots of total N_{tot} (a, d), IWC (b, e) and LWC (c, f) produced by CNTRL~~
 846 ~~(top panel) and PHILL (bottom panel) simulations between 26 January and 1 February 2014.~~
 847 ~~The height is given in km a.g.l.~~
 848

849
 850 Focusing on the ice-seeding event of 26 January, the enhanced aggregation rate observed
 851 at heights above ~ 2.5 km in the atmosphere indicates the enhanced collision efficiencies of the
 852 precipitating ice particles while falling from the seeder cloud (Fig. 6c). Note that a portion of
 853 the sedimented ice particles sublimates before reaching the feeder cloud at heights ~ 3 -5 km,
 854 indicating the prevailing unsaturated conditions in this layer (Fig. 6b). Within this layer the
 855 aggregation of snowflakes weakens, while it is enhanced again when the falling hydrometeors
 856 enter the feeder cloud. The bottom line is that, even under the simulated seeder-feeder events
 857 the concentrations of ice particles reaching the ground in CNTRL simulation remain severely
 858 underestimated (Section 3.1). Despite the low concentrations of ice crystals simulated by the
 859 CNTRL simulation, the low-level cloud is glaciated more frequently during the SE_ than during
 860 the NW_ winds case (Fig. 5c). This is probably because of the higher updraft velocities
 861 prevailing until 28 January (Fig. 2d), preventing ice crystals from falling through the lower
 862 parts of the cloud (Lohmann et al., 2016).
 863



864
 865 **Figure 6.** Vertical profiles of (a, d) primary and secondary ice production, (b, e) riming and
 866 vapor deposition or sublimation and (c, f) snow aggregation produced by the CNTRL (top
 867 panel) and PHILL (bottom panel) simulations at 17:00 UTC on 26 January (solid line) and at
 868 19:00 UTC on 30 January (dashed line). The vertical profile of simulated temperature is also
 869 superimposed in (a). The cloud liquid water content (Q_c) is shown in panels (b and c) to
 870 represent the tendency due to riming, while the mass mixing ratio of the ice and snow species
 871 ($Q_i + Q_s$), are representing the relative tendencies due to vapor deposition or sublimation. Note
 872 that the tendencies due to snow aggregation in (c, f) are presented in absolute values. The height
 873 is given in km a.g.l.

874 Activating the BR mechanism along with the seeding of precipitating hydrometeors in
 875 PHILL simulation shifts the simulated N_{isg} towards higher concentrations that are found to
 876 exceed 300 L^{-1} in the lower-level part of the cloud (Fig. 5d). On 26 January the mode of the
 877 cloud ice distribution shifts to slightly bigger sizes, while on 30 January the modal sizes
 878 become almost an order of magnitude smaller compared with the CNTRL simulation
 879 (supplement Fig. S4). The enhanced concentrations of bigger ice particles simulated in the first
 880 case experience rapid growth through vapor deposition and riming (Fig. 6e) causing a slight
 881 increase in the simulated IWC (Fig. 5e) at the expense of the surrounding cloud droplets in the
 882 low-level feeder cloud (Fig. 5f). Nevertheless, the smaller ice particles simulated in the second
 883 case grow less efficiently through vapor deposition, while the explosive multiplication of ice
 884 through BR seems to fully glaciate the low-level cloud below ~ 1 km resulting in an almost zero
 885 riming rate (Fig. 6e). The reduced primary ice production rate observed during both case
 886 studies is a consequence of the depletion of liquid water when BR is considered (Fig. 6d). A
 887 suppression of heterogeneous ice nucleation following the introduction of SIP into models has

Formatted: Font: 12 pt, Not Italic, Font color: Text 1

888 [already been reported in previous studies \(Phillips et al., 2017b; Dedekind et al., 2021; Zhao](#)
889 [and Liu, 2021b\).](#)

890 The key difference between CNTRL and PHILL simulations is that the latter takes
891 advantage of the enhanced ice particle growth through aggregation while falling to the feeder
892 cloud below ~2 km, -where large snowflakes coexist with smaller ice crystals (Fig. 4a, 6a, 6d).
893 This allows for differential settling, which enhances collision efficiency facilitating ice
894 multiplication through BR. This is the reason why the vertical profile of secondary ice
895 formation agrees with the corresponding profile of aggregation during both case studies (Fig.
896 6d, 6f). On 26 January the first secondary ice particles start forming already within the seeder
897 cloud with the contribution of SIP increasing considerably when reaching the feeder cloud,
898 where the tendency due to SIP is more than 3 orders of magnitude higher than primary ice
899 production (Fig. 6d). The significant role of SIP stands out also on 30 January at altitudes below
900 2 km. It is, therefore, essential to consider SIP though BR in the feeder cloud, in order to
901 achieve the enhanced levels of ICNCs frequently observed within seeder-feeder events in the
902 alpine region. This is in agreement with the observational study of Ramelli et al. (2021) on an
903 ice-seeding case occurring in the region around Davos in the Swiss Alps. In this study, they
904 proposed that SIP though HM and BR were necessary to explain the elevated ICNCs in feeder
905 clouds.

906 A classification of the dominant type of precipitation was applied to the polarimetric data
907 collected by a weather radar deployed at the Kleine Scheidegg station (2061 m a.s.l) during the
908 SE case between 30 and 31 January (supplement Fig. S6). In the derived time series, we can
909 identify periods when individual ice crystals (not aggregated and not significantly rimed)
910 dominate over the entire precipitation column followed by periods when a clear stratification
911 is present with ice crystals aloft and mostly aggregates and rimed ice particles below. This
912 stratification is observed on 30 January at 19:00 UTC when the model tendencies are extracted
913 (dashed lines in Fig. 6). Allowing for the BR process in PHILL ~~simulation~~ results in a 2 orders
914 of magnitude enhancement in the aggregation rates close to the ground, which can better
915 reproduce the signatures observed in the hydrometeor classification at that time. An increase
916 in the simulated aggregates and rimed particles is expected to increase orographic precipitation,
917 which is important given that these low-level feeder clouds are incapable of producing
918 significant amounts of precipitation. Indeed, the mean surface precipitation produced by
919 PHILL is 30% (10%) increased during the NW (SE) case compared with CNTRL ([supplement](#)
920 [Fig. S7](#)), which is in contrast to Dedekind et al. (2021) where the activation of the BR process
921 is found to suppress the regions of strong surface precipitation. This was attributed to the

Formatted: Font color: Black

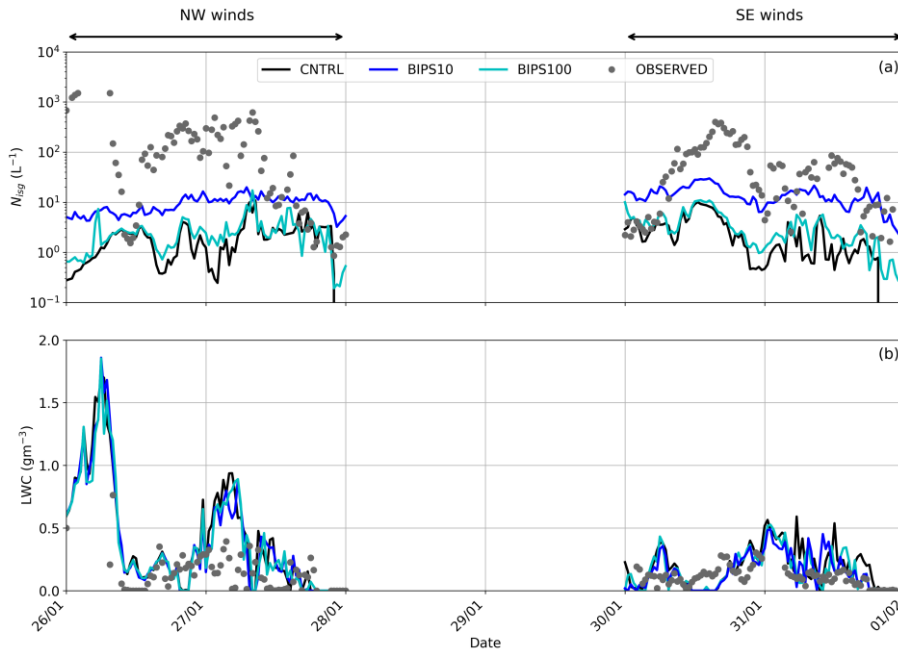
922 limited efficiency of the small secondary ice particles to grow sufficiently to precipitation sizes
923 when the local updrafts lift them to the upper parts of the cloud that were glaciated. The radar-
924 based hydrometeor classification reveals also the predominance of ice crystals at the beginning
925 and the end of the precipitating periods (e.g., on 30 January at 15:00-17:30 or 31 January at
926 04:30-06:00), which is again more consistent with the vertical profile of N_i produced by PHILL
927 rather than the CNTRL simulation (supplement Fig. S6, S8).

928

929 3.2 Sensitivity to the injection of ice crystals from the surface

930 In this section we examine if the surface-originating small ice particles could have the potential
931 to initiate and enhance ice particle growth in the near-surface MPCs present in our case studies.
932 Fig. 7 illustrates two additional WRF simulations – BIPS10 and BIPS100 – where the ice
933 crystal source applied to the first model level is equal to 10 and 100 L^{-1} , respectively (Table 2).
934 Note that these two sensitivity tests do not consider any SIP process to analyze the influence
935 of BIPS only. The total N_{isg} values produced in BIPS10 are only slightly increased compared
936 to the CNTRL simulation and generally remain outside the observed range at JFJ (Fig. 7a). An
937 order of magnitude increase in the applied NBIPS is seen to enhance the modeled N_{isg} during
938 both case studies, however our simulations are still lacking ice particles. This is particularly
939 evident during the NW winds case, where the simulated N_{isg} varies most of the time around 10
940 L^{-1} , remaining an order of magnitude lower than the observations. During the SE case, the
941 model performance is slightly improved with the N_{isg} reaching up to $\sim 25 L^{-1}$ in BIPS100, which
942 occasionally falls within the lower limit of the observed ICNC values (e.g., in the evening of
943 31 January). At times when the detected ICNCs remain quite low (i.e., on the order of 10 L^{-1}),
944 the contribution of blowing snow particles probably from the Aletsch Glacier is sufficient to
945 explain the observations at JFJ.

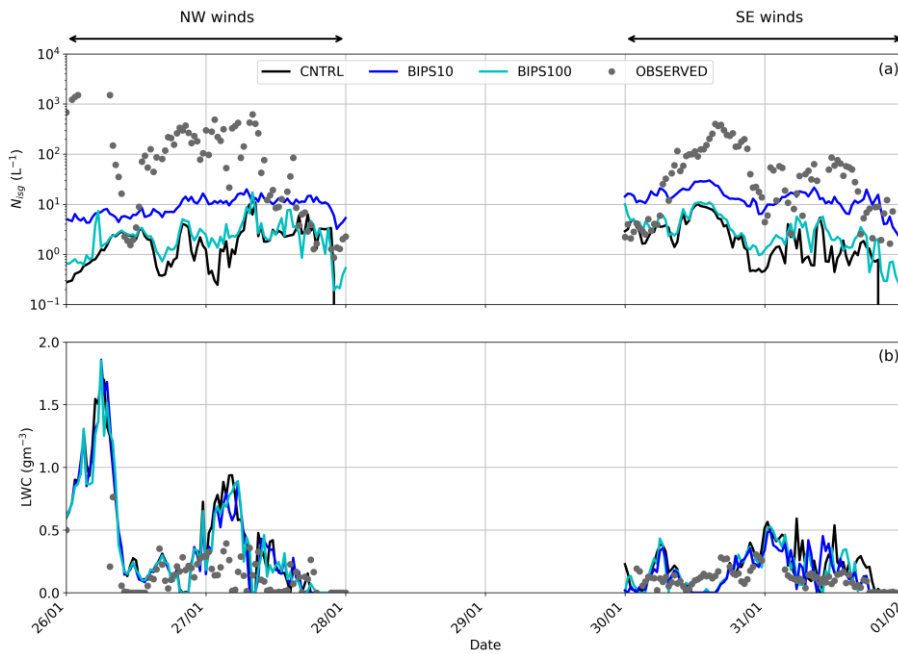
946



947 **Figure 7.** Time series of (a) total N_{iss} and (b) LWC, predicted between 26 January and 1
 948 February 2014 by the two sensitivity simulations accounting for the effect of blowing snow,
 949 BIPS10 (cyan line) and BIPS100 (blue line).
 950

951
 952 As indicated in Fig. 7b, during the NW flow the simulated LWC at the first model level
 953 in BIPS10 and BIPS100 almost coincides with the CNTRL simulation of WRF. The three
 954 sensitivity simulations are producing comparable median and quartile LWC values (Table 5),
 955 with BIPS10 and BIPS100 producing median LWC values closer to the observed ones during
 956 the SE flow. When comparing against the LWC values in the third quartile though, the two
 957 simulations lead to an overestimation up to a factor of ~ 1.5 during both case studies. Given that
 958 there is approximately a factor of >20 (5) difference between the modeled and observed ICNCs
 959 during the NW (SE) winds case (Table 3), Fig. 7 overall reveals that the addition of a source
 960 of ice crystals from the effect of blowing snow cannot account for the observed liquid-ice phase
 961 partitioning in the simulated orographic MPCs.

Formatted: Indent: First line: 0 cm



963 **Figure 7.** Time series of (a) total N_{isg} and (b) LWC, predicted between 26 January and 1
 964 February 2014 by the two sensitivity simulations accounting for the effect of blowing snow,
 965 BIPS10 (cyan line) and BIPS100 (blue line).
 966

967
 968 Our findings are in contrast with the modeling study of Farrington et al. (2016), where a
 969 different approach was proposed to include the surface effect on the ICNCs simulated with
 970 WRF. In this study, a single model domain was used with a horizontal resolution of 1 km. To
 971 account for the flux of hoar crystals being detached from the surface by mechanical fracturing,
 972 Farrington et al. (2016) included a wind-dependent surface flux of frost flowers adapted from
 973 Xu et al. (2013). Despite the improved performance of ~~the WRF model~~ in terms of predicted
 974 ICNCs and LWC, the wind-dependent formulation of the surface flux caused the modeled
 975 ICNCs to become strongly correlated with the simulated horizontal wind speed – a behavior
 976 that was not confirmed by the observations of Lloyd et al. (2015). Nonetheless, the highest
 977 observed ICNCs at the beginning of the NW case correspond to the time when both the
 978 observed and modeled wind speed is the strongest (Fig. 2c), implying that a wind-dependent
 979 surface flux of BIPS could potentially elevate the simulated N_{isg} to the observed levels at this
 980 time.
 981

Formatted: Indent: First line: 0 cm

982 3.3 The synergistic impact of BR and surface-induced ice crystals

983 It is deducible from the above discussion that the sole inclusion of a constant source of BIPS
984 in our simulations cannot efficiently bridge the gap between modeled and measured ICNCs.
985 Our aim in this section is to explore the combined effect of SIP through BR and blowing snow
986 on the simulated orographic MPCs, since both processes are deemed to be important when
987 trying to explain the high ICNCs observed in alpine environments. This is addressed in the
988 final sensitivity simulation, BIPS100_PHILL, the results of which are compared with the
989 CNTRL and PHILL simulations in Fig. 8.

990 In terms of the modeled ice particle concentrations, the combination of the simplified
991 blowing snow treatment and BR parameterization can account for most of the discrepancy
992 between modeled and observed ICNCs, particularly during the SE case (Fig. 8a), when the
993 simulation leads to best agreement with the observed interquartile values (Table 3).
994 BIPS100_PHILL and CNTRL generally differ by an average factor of ~ 100 (40) during the
995 NW (SE) case, with the former producing N_{isg} values that are sometimes elevated by up to ~ 3
996 (2) orders of magnitude (Fig. 8a). Compared to the PHILL setup, including a source of BIPS
997 is found to improve the modeled ICNCs close to the surface episodically – for instance in the
998 evening of 30 and 31 January, with the N_{isg} in BIPS100_PHILL efficiently reaching the
999 observed levels (Fig. 8a). Note that BIPS can contribute to the modeled N_{isg} even without the
1000 presence of a near-surface orographic cloud (e.g., Geerts et al., 2015; Beck et al., 2018). For
1001 instance, BIPS100_PHILL is the only sensitivity simulation producing high N_{isg} values in the
1002 evening of 27 and 31 January, when the low-level cloud is dissipated (Fig. 5c, f). In the former
1003 case, however, the model results in an overestimate of the ICNCs, which is also observed
1004 during the early hours of 30 January, suggesting that the applied source of ice crystals is
1005 unrealistically high at this time.

1006

Formatted: Font color: Auto

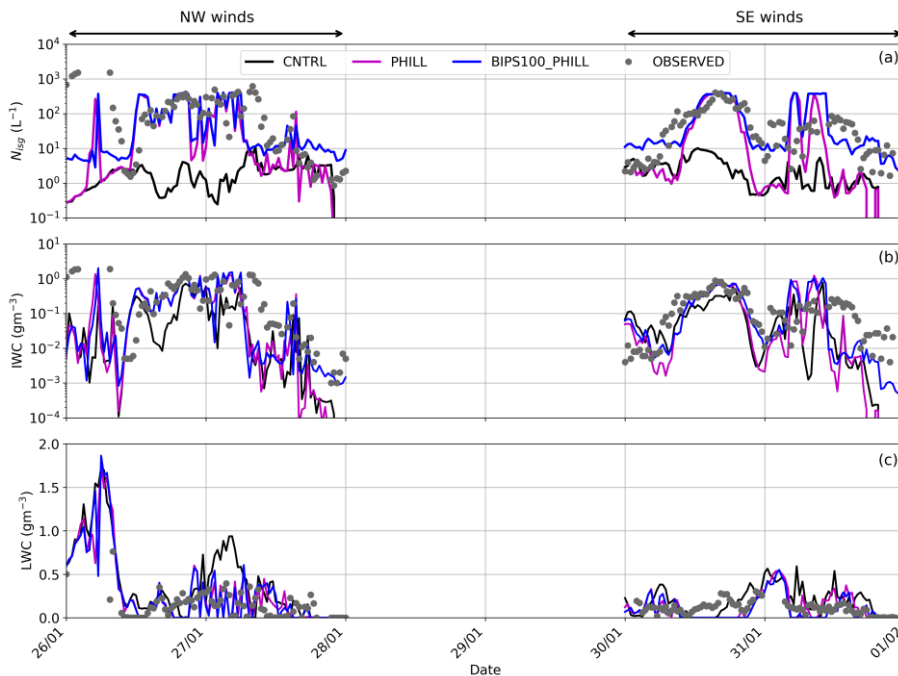
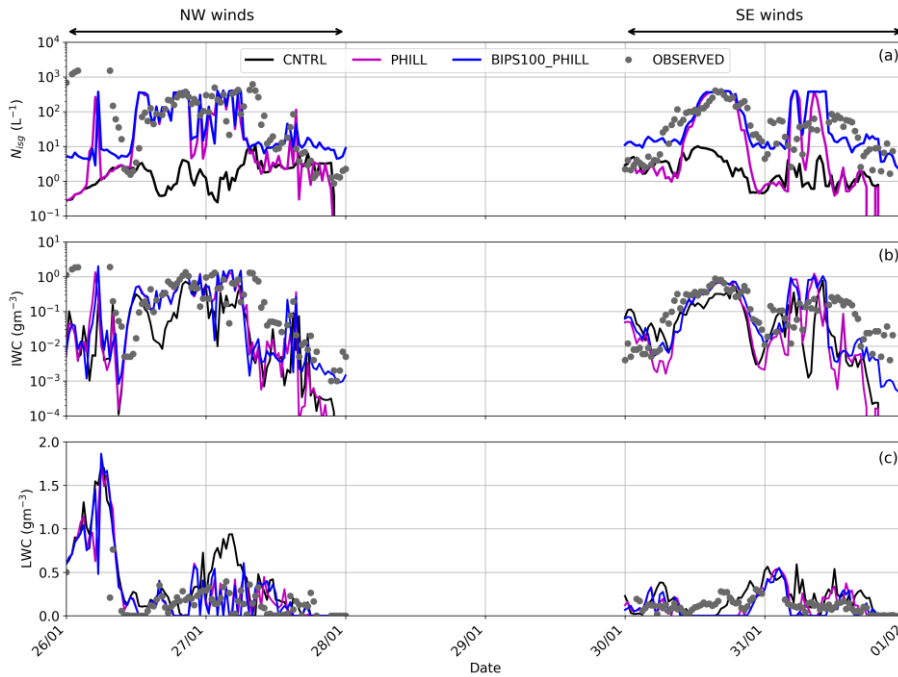


Figure 8. Time series of (a) total N_{isg} , (b) IWC and (c) LWC, predicted between 26 January and 1 February 2014 by the sensitivity simulation BIPS100 PHILL (blue line), which examines the combined effect of ice multiplication through BR and blowing snow.

As the mixed-phase conditions are sustained throughout both case studies (Fig. 8c), the plume of ice crystals is mixed into an ice-supersaturated environment and, thus, BIPS are expected to promote ice growth through their interaction with the surrounding supercooled liquid droplets and (ice) supersaturated air. The number of BIPS reaching the cloud base might not be large, but their presence is expected to further facilitate the action of the BR mechanism, considering the depositional growth they will undergo within the supercooled boundary layer cloud. This is illustrated for example with the concurrent increase in N_{isg} and IWC observed on 30 January at approximately 21:00 UTC (Fig. 8a, 8b) in the presence of the low-level cloud (Fig. 8c). Note that the elevated N_{isg} caused by the addition of BIPS is not always followed by an efficient increase in the simulated IWC. This can be observed for example on 27 January at 12:00 UTC or in the evening of 31 January (Fig. 8b).

Formatted: Font color: Auto

Formatted: Font color: Auto



1024 **Figure 8.** Time series of (a) total N_{isg} , (b) IWC and (c) LWC, predicted between 26 January
 1025 and 1 February 2014 by the sensitivity simulation BIPS100_PHILL (blue line), which
 1026 examines the combined effect of ice multiplication through BR and blowing snow
 1027
 1028

1029 A discrepancy between modeled and observed IWC was also highlighted in the study of
 1030 Farrington et al. (2016), and was attributed to the small sizes of the hoar frost particles assumed
 1031 (i.e., 10 μm). Although here BIPS are assumed to have sizes of 100 μm , still the
 1032 underestimation in the cloud IWC has not been overcome. This suggests that the applied source
 1033 of BIPS combined with the effect of SIP through BR shifts the ice particle spectra to smaller
 1034 sizes, which are not very efficient in riming and the WBF process and, thus, do not always
 1035 contribute to significant increases in IWC values. Overall, the interquartile values presented in
 1036 Table 4 reveal that BIPS100_PHILL and PHILL yield almost identical IWC values, suggesting
 1037 that the implementation of a constant source of BIPS does not further improve the
 1038 representation of the total ice mass despite the improvements in the simulated N_{isg} . Focusing
 1039 on the LWC values in the third quartile, though, including a source of BIPS results in better
 1040 agreement with the CLACE observations during the SE case, while it is shown to have little
 1041 effect on the cloud liquid phase during the NW case (Table 5). Despite the increase in the
 1042 modeled N_{isg} observed in BIPS100_PHILL especially during the SE case, the liquid water in

Formatted: Font color: Auto

1043 the low-level orographic cloud is not further depleted (Fig. 8c). This is presumably because the
1044 mean surface precipitation produced is also enhanced by almost ~20% compared to PHILL
1045 (supplement Fig. S7), which seems to balance the excessive ice production.

1046 One final point that is worth noting here is that there are still some certain periods when
1047 BIPS100_PHILL fails to reproduce the observed range of ICNCs. This could imply the
1048 potential contribution of additional ice multiplication processes to the observed ice particle
1049 concentrations. Indeed, the seeder-feeder configuration observed in the examined case studies
1050 could favor the fragmentation of sublimating hydrometeors while falling through an
1051 subsaturated environment before entering the feeder cloud (e.g., Bacon et al., 1998). The so-
1052 called “sublimational break-up” is an overlooked SIP process which is not yet described in the
1053 M05 scheme. Also, note that the periods when the modeled ICNCs remain below the observed
1054 ice number levels are mainly identified when the simulated temperature drops below $-15\text{ }^{\circ}\text{C}$
1055 and the wind speed exceeds 10 ms^{-1} or even 20 ms^{-1} (e.g., in the morning of 26 January or 27
1056 January at around 12:00 UTC). This is when the incorporation of surface-based processes
1057 becomes of primary importance. The simplified methodology we followed here although
1058 instructive, yet it faces several limitations. For instance, the constant source of BIPS is
1059 sometimes found to overestimate the modeled N_{isg} and IWC. In order to accurately assess the
1060 potential role of the snow-covered surfaces in elevating the simulated ICNCs, an improved
1061 spatio-temporal description of the concentration and distribution of BIPS is required.
1062 Furthermore, the applied ice crystal source is independent of some key parameters controlling
1063 its resuspension, such as the horizontal wind speed, the updrafts or the friction velocity (e.g.,
1064 Vionnet et al., 2013, 2014). For example, in the early morning hours of 26 January, the high
1065 simulated horizontal and vertical velocities (Fig. 2c, 2d) are expected to loft significant BIPS
1066 concentrations into the cloud layer, owing to enhanced mechanical mixing and momentum flux
1067 close to the surface. Nonetheless, the contribution of the induced plume of BIPS remains
1068 constant throughout the NW case study (Fig. 7a), which seems to lead to an underestimation
1069 of the total ice particle concentration and mass. A more realistic parameterization of the BIPS
1070 flux or the coupling with a detailed snowpack model would, therefore, be essential for a more
1071 accurate representation of the effect of blowing snow.

1072

1073 **4. Summary and conclusions**

1074 This study employs the mesoscale model WRF to explore the potential impact of ice
1075 multiplication processes on the liquid-ice phase partitioning in the orographic MPCs observed

1076 during the CLACE 2014 campaign at the mountain-top site of JFJ in the Swiss Alps. The
1077 orography surrounding JFJ channels the direction of the horizontal wind speed, giving us the
1078 opportunity to analyze two frontal cases occurring under NW and SE conditions.

1079 DS and BR mechanisms were implemented in the default M05 scheme in WRF, in
1080 addition to the HM parameterization, which however remained inactive in the simulated
1081 temperature range (-10 to -24 °C). The DS process is parameterized following either the latest
1082 theoretical formulation developed by Phillips et al. (2018) or the more simplified
1083 parameterization proposed by Sullivan et al. (2018a). Our sensitivity simulations revealed that
1084 the DS mechanism is ineffective in the two considered alpine MPCs, even under the higher
1085 updraft velocity conditions associated with the NW winds case study. ~~This is due, owing to~~
1086 ~~the lack of sufficiently big raindrops, necessary to initiate this~~ large drops required for the
1087 process.

1088 To parameterize the number of fragments generated per ice-ice collision we followed
1089 again two different approaches: either the simplified temperature dependent formulation of
1090 Takahashi et al. (1995) scaled for the size of the particle that undergo fragmentation
1091 (Sotiropoulou et al., 2021a) or the more advanced physically-based Phillips et al. (2017a)
1092 parameterization. It is important to apply the Takahashi parameterization only to consider
1093 collisions between rimed ice particles, otherwise the number of generated fragments is
1094 significantly overestimated. Including a description of the BR mechanism is essential for
1095 reproducing the ICNCs observed in the simulated orographic clouds, especially at temperatures
1096 higher than ~ -15 °C, where INPs are generally sparse. SIP through BR is found to enhance the
1097 modeled ICNCs by up to 3 (2) orders of magnitude during the NW (SE) case, improving the
1098 model agreement with observations. This ice enhancement can cause up to an order of
1099 magnitude increase in the mean simulated IWC values compared with the CNTRL simulation,
1100 which is attributed to the enhanced ice crystal growth and cloud-ice-to-snow autoconversion.
1101 The increase in the simulated ICNCs also depletes the cloud LWC by at least a factor of 2
1102 during both cases, which is more consistent with the measured LWC values.

1103 One of the most interesting outcomes of this study is the association of the enhanced BR
1104 efficiency with the occurrence of in-cloud seeder-feeder events, which are commonly found in
1105 Switzerland (Proske et al., 2021). While ice-seeding situations are associated with enhanced
1106 orographic precipitation in the alpine region, the CNTRL simulation fails to reproduce the
1107 elevated ICNCs reaching the ground. The falling ice hydrometeors experience efficient growth
1108 through aggregation in the seeder part of the cloud, which is enhanced when reaching the feeder

1109 cloud at altitudes below 2 km, where primary ice crystals form and grow through vapor
1110 deposition and riming. Aggregation of snowflakes seems to be the major driver of secondary
1111 ice formation in the examined seeder-feeder events. SIP though BR is initiated already within
1112 the seeder cloud, while it becomes immensely important in the feeder cloud where its
1113 production rate exceeds the one of primary ice formation. The increased generation of
1114 secondary ice fragments does not always lead to ice explosion and cloud glaciation, as it is
1115 followed by an enhancement in the precipitation sink owing to a shift in the ice particle
1116 spectrum. Including a description of the BR mechanism is, therefore, crucial for explaining the
1117 ice particle concentration and mass observed in the low-level feeder clouds.

1118 To assess the potential role of blowing snow in the simulated orographic clouds, a
1119 constant source of ice crystals was introduced in the first atmospheric level of WRF. Our results
1120 indicate that blowing snow alone cannot explain the high ICNCs observed at JFJ, but when this
1121 source is combined with the BR mechanism then the gap between modeled and measured
1122 ICNCs is sufficiently bridged. The biggest influence of blowing snow is mainly detected at
1123 times when the simulated temperatures are low enough (< -15 °C), while the presence of a low-
1124 level cloud is required for SIP to manifest. The concentrations of BIPS reaching the cloud base
1125 are not high, but when they are mixed among supercooled liquid droplets they are expected to
1126 grow, facilitating ice multiplication through BR. Nonetheless, including a wind-dependence or
1127 a spatio-temporal variability in the applied ice crystal source would be essential to provide a
1128 more precise description of the effect of blowing snow on the simulated clouds.

1129 Overall, our findings indicate that outside the HM temperature range, a correct
1130 representation of both secondary ice (through BR) and an external ice seeding mechanism,
1131 which is primarily precipitating ice particles formed aloft and to a lesser degree wind-blown
1132 ice from the surface, ~~will improve the accuracy of the liquid-ice partitioning in MPCs predicted~~
1133 ~~by atmospheric numerical models. More precisely, the implementation of SIP through BR can~~
1134 ~~effectively shift the number concentrations of ice particles in the right direction dictated by~~
1135 ~~observations of alpine MPCs, which is in turn critical not only for the determination of their~~
1136 ~~optical properties but also for the accurate estimate of precipitation patterns~~ is fundamentally
1137 important for accurately predicting the liquid-ice partitioning and properties of MPCs. Given
1138 the high frequency of seeder-feeder events in orographic environments, including the new
1139 physics of BR may address a large source of predictive bias in atmospheric models.

1140

1141 *Code and data availability.* The WRF outputs presented in this study will be made available at
1142 <https://zenodo.org/>, while the updated Morrison scheme is available upon request. @Note by
1143 authors: Data will be made available upon acceptance of final publication.

1144

1145 *Competing interests.* The authors declare no conflict of interest.

1146

1147 *Author Contributions.* PG and AN conceived and led this study with input from GS. EV helped
1148 with the WRF configuration and setup. GS provided the updated microphysics scheme with
1149 the detailed BR parameterizations. PG implemented the DS parameterizations with help from
1150 GS, conducted the simulations, analyzed the results and, together with AN, wrote the main
1151 paper. All authors contributed to the scientific interpretation and writing of the paper.

1152

1153 *Acknowledgements.* The authors would like to thank Gary Lloyd for providing the
1154 microphysical measurements, as well as Jacopo Grazioli for collecting and pre-processing the
1155 radar data. The authors are also thankful to Varun Sharma and Michael Lehning for the fruitful
1156 discussions on the contribution of blowing snow in the alpine region.

1157

1158 *Financial support.* This research has been supported by the Horizon 2020 project FORCeS
1159 (grant 821205) and the European Research Council project PyroTRACH (grant 726165). GS
1160 received funding from the Swedish Research Council for Sustainable Development FORMAS
1161 (project ID 2018-01760).

1162 [GS and AN acknowledge support by the European Union under the H2020 Marie Skłodowska-](#)
1163 [Curie Actions project SIMPHAC under grant agreement 898568.](#)

Formatted: Justified, Space After: 6 pt, Line spacing:
1,5 lines

1164 **References**

- 1165 Atlas, R. L., Bretherton, C. S., Blossey, P. N., Gettelman, A., Bardeen, C., Lin, P. and Ming,
1166 Y.: How Well Do Large-Eddy Simulations and Global Climate Models Represent
1167 Observed Boundary Layer Structures and Low Clouds Over the Summertime Southern
1168 Ocean?, *J. Adv. Model. Earth Syst.*, 12(11), 1–25, doi:10.1029/2020MS002205, 2020.
- 1169 Baltensperger, U., Schwikowski, M., Jost, D. T., Nyeki, S., Gäggeler, H. W. and Poulida, O.:
1170 Scavenging of atmospheric constituents in mixed phase clouds at the high-alpine site
1171 Jungfraujoch part I: Basic concept and aerosol scavenging by clouds, *Atmos. Environ.*, 32,
1172 3975–3983, doi:10.1016/S1352-2310(98)00051-X, 1998.
- 1173 Beck, A., Henneberger, J., Fugal, J. P., David, R. O., Lacher, L. and Lohmann, U.: Impact of
1174 surface and near-surface processes on ice crystal concentrations measured at mountain-top
1175 research stations, *Atmos. Chem. Phys.*, 18(12), 8909–8927, doi:10.5194/acp-18-8909-
1176 2018, 2018.
- 1177 Beheng, K. D.: Microphysical Properties of Glaciating Cumulus Clouds: Comparison of
1178 Measurements With A Numerical Simulation, *Q. J. R. Meteorol. Soc.*, 113(478), 1377–
1179 1382, doi:10.1002/qj.49711347815, 1987.
- 1180 Bergeron, T.: On the physics of clouds and precipitation, *Proc. 5th Assembly UGGI*, 1935,
1181 Lisbon, Portugal, 156–180, 1935.
- 1182 Bigg, E. K.: The supercooling of water, *Proc. Phys. Soc. Sect. B*, 66(8), 688–694,
1183 doi:10.1088/0370-1301/66/8/309, 1953.
- 1184 Brown, P. R. A. and Francis, P. N.: Improved Measurements of the Ice Water Content in Cirrus
1185 Using a Total-Water Probe, *J. Atmos. Ocean. Technol.*, 12, 410–414, doi:10.1175/1520-
1186 0426(1995)012<0410:IMOTIW>2.0.CO;2, 1995.
- 1187 Browning, K. A., Hill, F. F. and Pardoe, C. W.: Structure and mechanism of precipitation and
1188 the effect of orography in a wintertime warm sector, *Q. J. R. Meteorol. Soc.*, 100(425),
1189 309–330, doi:10.1002/qj.49710042505, 1974.
- 1190 Browning, K. A., Pardoe, C. W. and Hill, F. F.: The nature of orographic rain at wintertime
1191 cold fronts, *Q. J. R. Meteorol. Soc.*, 101(428), 333–352, doi:10.1002/qj.49710142815,
1192 1975.
- 1193 Chen, F. and Dudhia, J.: Coupling and advanced land surface-hydrology model with the Penn
1194 State-NCAR MM5 modeling system. Part I: Model implementation and sensitivity, *Mon.*
1195 *Weather Rev.*, 129(4), 569–585, doi:10.1175/1520-
1196 0493(2001)129<0569:CAALSH>2.0.CO;2, 2001.

1197 Chou, C., Stetzer, O., Weingartner, E., Jurányi, Z., Kanji, Z. A. and Lohmann, U.: Ice nuclei
 1198 properties within a Saharan dust event at the Jungfraujoch in the Swiss Alps, *Atmos.*
 1199 *Chem. Phys.*, 11, 4725–4738, doi:10.5194/acp-11-4725-2011, 2011.

1200 Choulaton, T. W., Griggs, D. J., Humood, B. Y. and Latham, J.: Laboratory studies of riming,
 1201 and its relation to ice splinter production, *Q. J. R. Meteorol. Soc.*, 106(448), 367–374,
 1202 doi:10.1002/qj.49710644809, 1980.

1203 Choulaton, T. W., Bower, K. N., Weingartner, E., Crawford, I., Coe, H., Gallagher, M. W.,
 1204 Flynn, M., Crosier, J., Connolly, P., Targino, A., Alfarra, M. R., Baltensperger, U.,
 1205 Sjogren, S., Verheggen, B., Cozic, J. and Gysel, M.: The influence of small aerosol
 1206 particles on the properties of water and ice clouds, *Faraday Discuss.*, 137, 205–222,
 1207 doi:10.1039/b702722m, 2008.

1208 Chow, F. K., De Wekker, Stephan, F. J., and Snyder, B. J.: Mountain weather research and
 1209 forecasting: recent progress and current challenges, Springer, Dordrecht, the Netherlands,
 1210 2013.

1211 Conen, F., Rodríguez, S., Hüglin, C., Henne, S., Herrmann, E., Bukowiecki, N. and Alewell,
 1212 C.: Atmospheric ice nuclei at the high-altitude observatory Jungfraujoch, Switzerland,
 1213 *Tellus, Ser. B Chem. Phys. Meteorol.*, 67(1), doi:10.3402/tellusb.v67.25014, 2015.

1214 Cooper, W. A.: Ice initiation in natural clouds, *Meteor. Mon.*, 21, 29–32,
 1215 <https://doi.org/10.1175/0065-9401-21.43.29>, 1986.

1216 Crosier, J., Bower, K. N., Choulaton, T. W., Westbrook, C. D., Connolly, P. J., Cui, Z. Q.,
 1217 Crawford, I. P., Capes, G. L., Coe, H., Dorsey, J. R., Williams, P. I., Illingworth, A. J.,
 1218 Gallagher, M. W. and Blyth, A. M.: Observations of ice multiplication in a weakly
 1219 convective cell embedded in supercooled mid-level stratus, *Atmos. Chem. Phys.*, 11(1),
 1220 257–273, doi:10.5194/acp-11-257-2011, 2011.

1221 Dedekind, Z., Lauber, A., Ferrachat, S., and Lohmann, U.: Sensitivity of precipitation
 1222 formation to secondary ice production in winter orographic mixed-phase clouds, *Atmos.*
 1223 *Chem. Phys. Discuss., (February), 1–27*, 21, 15115–15134, [https://doi.org/10.5194/acp-](https://doi.org/10.5194/acp-2020-132621-15115-2021)
 1224 [2020-132621-15115-2021](https://doi.org/10.5194/acp-2020-132621-15115-2021), 2021.

1225 Déry, S. J. and Yau, M. K.: A climatology of adverse winter-type weather events, *J. Geophys.*
 1226 *Res. Atmos.*, 104(D14), 16657–16672, doi:10.1029/1999JD900158, 1999.

1227 Farrington, R. J., Connolly, P. J., Lloyd, G., Bower, K. N., Flynn, M. J., Gallagher, M. W.,
 1228 Field, P. R., Dearden, C. and Choulaton, T. W.: Comparing model and measured ice
 1229 crystal concentrations in orographic clouds during the INUPIAQ campaign, *Atmos. Chem.*
 1230 *Phys.*, 16(8), 4945–4966, doi:10.5194/acp-16-4945-2016, 2016.

1231 Field, P. R. and Heymsfield, A. J.: Importance of snow to global precipitation, *Geophys. Res.*
1232 *Lett.*, 42(21), 9512–9520, doi:10.1002/2015GL065497, 2015.

1233 Field, P. R., Lawson, R. P., Brown, P. R. A., Lloyd, G., Westbrook, C., Moisseev, D.,
1234 Miltenberger, A., Nenes, A., Blyth, A., Choullarton, T., Connolly, P., Buehl, J., Crosier, J.,
1235 Cui, Z., Dearden, C., DeMott, P., Flossmann, A., Heymsfield, A., Huang, Y., Kalesse, H.,
1236 Kanji, Z. A., Korolev, A., Kirchgaessner, A., Lasher-Trapp, S., Leisner, T., McFarquhar,
1237 G., Phillips, V., Stith, J. and Sullivan, S.: Chapter 7. Secondary Ice Production - current
1238 state of the science and recommendations for the future, *Meteorol. Monogr.*, 58,
1239 doi:10.1175/amsmonographs-d-16-0014.1, 2017.

1240 Findeisen, W.: Die kolloidmeteorologischen vorgänge bei der niederschlagsbildung, *Meteorol.*
1241 *Z.*, 55, 121–133, 1938.

1242 Fridlind, A. M., Ackerman, A. S., McFarquhar, G., Zhang, G., Poellot, M. R., DeMott, P. J.,
1243 Prenni, A. J. and Heymsfield, A. J.: Ice properties of single-layer stratocumulus during the
1244 Mixed-Phase Arctic Cloud Experiment: 2. Model results, *J. Geophys. Res. Atmos.*,
1245 112(24), 1–25, doi:10.1029/2007JD008646, 2007.

1246 Fu, S., Deng, X., Shupe, M. D. and Xue, H.: A modelling study of the continuous ice formation
1247 in an autumnal Arctic mixed-phase cloud case, *Atmos. Res.*, 228(March), 77–85,
1248 doi:10.1016/j.atmosres.2019.05.021, 2019.

1249 Geerts, B., Pokharel, B. and Kristovich, D. A. R.: Blowing snow as a natural glaciogenic cloud
1250 seeding mechanism, *Mon. Weather Rev.*, 143(12), 5017–5033, doi:10.1175/MWR-D-15-
1251 0241.1, 2015.

1252 Grazioli, J., Lloyd, G., Panziera, L., Hoyle, C. R., Connolly, P. J., Henneberger, J. and Berne,
1253 A.: Polarimetric radar and in situ observations of riming and snowfall microphysics during
1254 CLACE 2014, *Atmos. Chem. Phys.*, 15, 13787–13802, doi:10.5194/acp-15-13787-2015,
1255 2015.

1256 Griggs, D. J. and Choullarton, T. W.: Freezing modes of riming droplets with application to ice
1257 splinter production, *Q. J. R. Meteorol. Soc.*, 109(459), 243–253,
1258 doi:10.1002/qj.49710945912, 1983.

1259 Griggs, D. J. and Choullarton, T. W.: A laboratory study of secondary ice particle production
1260 by the fragmentation of rime and vapour-grown ice crystals, *Q. J. R. Meteorol. Soc.*,
1261 112(471), 149–163, doi:10.1256/smsqj.47108, 1986.

1262 Hallett, J. and Mossop, S. C.: Production of secondary ice particles during the riming process,
1263 *Nature*, 249, 26–28, doi:10.1038/249026a0, 1974.

1264 Harris, L. M. and Durran, D. R.: An Idealized Comparison of One-Way and Two-Way Grid

1265 Nesting, *Mon. Weather Rev.*, 138(6), 2174–2187, doi:10.1175/2010MWR3080.1, 2010.

1266 Henneberg, O., Henneberger, J. and Lohmann, U.: Formation and development of orographic
1267 mixed-phase clouds, *J. Atmos. Sci.*, 74(11), 3703–3724, doi:10.1175/JAS-D-16-0348.1,
1268 2017.

1269 Hersbach, H., Bell, B., Berrisford, P., Hirahara, S., Horányi, A., Muñoz-Sabater, J., Nicolas,
1270 J., Peubey, C., Radu, R., Schepers, D., Simmons, A., Soci, C., Abdalla, S., Abellan, X.,
1271 Balsamo, G., Bechtold, P., Biavati, G., Bidlot, J., Bonavita, M., De Chiara, G., Dahlgren,
1272 P., Dee, D., Diamantakis, M., Dragani, R., Flemming, J., Forbes, R., Fuentes, M., Geer,
1273 A., Haimberger, L., Healy, S., Hogan, R. J., Hólm, E., Janisková, M., Keeley, S., Laloyaux,
1274 P., Lopez, P., Lupu, C., Radnoti, G., de Rosnay, P., Rozum, I., Vamborg, F., Villaume, S.
1275 and Thépaut, J. N.: The ERA5 global reanalysis, *Q. J. R. Meteorol. Soc.*, 146(730), 1999–
1276 2049, doi:10.1002/qj.3803, 2020.

1277 Heymsfield, A. J. and Mossop, S. C.: Temperature dependence of secondary ice crystal
1278 production during soft hail growth by riming, *Q. J. R. Meteorol. Soc.*, 110(465), 765–770,
1279 doi:10.1002/qj.49711046512, 1984.

1280 Heymsfield, A. J., Schmitt, C., Bansemer, A. and Twohy, C. H.: Improved representation of
1281 ice particle masses based on observations in natural clouds, *J. Atmos. Sci.*, 67(10), 3303–
1282 3318, doi:10.1175/2010JAS3507.1, 2010.

1283 Hoarau, T., Pinty, J. P. and Barthe, C.: A representation of the collisional ice break-up process
1284 in the two-moment microphysics LIMA v1.0 scheme of Meso-NH, *Geosci. Model Dev.*,
1285 11(10), 4269–4289, doi:10.5194/gmd-11-4269-2018, 2018.

1286 Hoose, C. and Möhler, O.: Heterogeneous ice nucleation on atmospheric aerosols: A review of
1287 results from laboratory experiments., 2012.

1288 James, R. L., Phillips, V. T. J., and Connolly, P. J.: Secondary ice production during the break-
1289 up of freezing water drops on impact with ice particles, *Atmos. Chem. Phys.* ~~Discuss.~~
1290 ~~[preprint], <https://doi.org/10.5194/acp-21-18519-2021-557>, in~~
1291 ~~review~~, 2021.

1292 Janjić, Z. I.: Nonsingular Implementation of the Mellor-Yamada Level 2.5 Scheme in the
1293 NCEP Meso model, NOAA/NWS/NCEP Off. note 437, 61 pp, 2002.

1294 Ikawa, M. and Saito, K.: Description of a Non-hydrostatic Model Developed at the Forecast
1295 Research Department of the MR, MRI Tech. Rep. 28, 238 pp., 1991.

1296 Kanji, Z. A., Ladino, L. A., Wex, H., Boose, Y., Burkert-Kohn, M., Cziczo, D. J. and Krämer,
1297 M.: Overview of Ice Nucleating Particles, *Meteorol. Monogr.*, 58, 1.1-1.33,
1298 doi:10.1175/amsmonographs-d-16-0006.1, 2017.

1299 Keinert, A., Spannagel, D., Leisner, T. and Kiselev, A.: Secondary ice production upon
1300 freezing of freely falling drizzle droplets, *J. Atmos. Sci.*, 77(8), 2959–2967,
1301 doi:10.1175/JAS-D-20-0081.1, 2020.

1302 Ketterer, C., Zieger, P., Bukowiecki, N., Collaud Coen, M., Maier, O., Ruffieux, D. and
1303 Weingartner, E.: Investigation of the Planetary Boundary Layer in the Swiss Alps Using
1304 Remote Sensing and In Situ Measurements, *Boundary-Layer Meteorol.*, 151(2), 317–334,
1305 doi:10.1007/s10546-013-9897-8, 2014.

1306 Kleinheins, J., Kiselev, A., Keinert, A., Kind, M. and Leisner, T.: Thermal imaging of freezing
1307 drizzle droplets: pressure release events as a source of secondary ice particles, *J. Atmos.*
1308 *Sci.*, 1–28, doi:10.1175/jas-d-20-0323.1, 2021.

1309 Korolev, A. and Isaac, G.: Phase transformation of mixed-phase clouds, *Q. J. R. Meteorol.*
1310 *Soc.*, 129(587 PART A), 19–38, doi:10.1256/qj.01.203, 2003.

1311 Korolev, A. and Leisner, T.: Review of experimental studies of secondary ice production.,
1312 2020.

1313 Korolev, A., McFarquhar, G., Field, P. R., Franklin, C., Lawson, P., Wang, Z., Williams, E.,
1314 Abel, S. J., Axisa, D., Borrmann, S., Crosier, J., Fugal, J., Krämer, M., Lohmann, U.,
1315 Schenczek, O., Schnaiter, M. and Wendisch, M.: Mixed-Phase Clouds: Progress and
1316 Challenges, *Meteorol. Monogr.*, 58, 5.1-5.50, doi:10.1175/amsmonographs-d-17-0001.1,
1317 2017.

1318 Korolev, A., Heckman, I., Wolde, M., Ackerman, A. S., Fridlind, A. M., Ladino, L. A., Paul
1319 Lawson, R., Milbrandt, J. and Williams, E.: A new look at the environmental conditions
1320 favorable to secondary ice production, *Atmos. Chem. Phys.*, 20(3), 1391–1429,
1321 doi:10.5194/acp-20-1391-2020, 2020.

1322 Korolev, A. V., Emery, E. F., Strapp, J. W., Cober, S. G., Isaac, G. A., Wasey, M. and Marcotte,
1323 D.: Small ice particles in tropospheric clouds: Fact or artifact? Airborne icing
1324 instrumentation evaluation experiment, *Bull. Am. Meteorol. Soc.*, 92(8), 967–973,
1325 doi:10.1175/2010BAMS3141.1, 2011.

1326 [Krinner, G., Derksen, C., Essery, R., Flanner, M., Hagemann, S., Clark, M., Hall, A., Rott, H.,](#)
1327 [Brutel-Vuilmet, C., Kim, H., Ménard, C. B., Mudryk, L., Thackeray, C., Wang, L.,](#)
1328 [Arduini, G., Balsamo, G., Bartlett, P., Boike, J., Boone, A., Chéruy, F., Colin, J., Cuntz,](#)
1329 [M., Dai, Y., Decharme, B., Derry, J., Ducharme, A., Dutra, E., Fang, X., Fierz, C., Ghattas,](#)
1330 [J., Gusev, Y., Haverd, V., Kontu, A., Lafaysse, M., Law, R., Lawrence, D., Li, W., Marke,](#)
1331 [T., Marks, D., Ménégoz, M., Nasonova, O., Nitta, T., Niwano, M., Pomeroy, J., Raleigh,](#)
1332 [M. S., Schaedler, G., Semenov, V., Smirnova, T. G., Stacke, T., Strasser, U., Svenson, S.,](#)

- 1333 [Turkov, D., Wang, T., Wever, N., Yuan, H., Zhou, W., and Zhu, D.: ESM-SnowMIP:](#)
1334 [assessing snow models and quantifying snow-related climate feedbacks, *Geosci. Model*](#)
1335 [Dev., 11, 5027–5049, <https://doi.org/10.5194/gmd-11-5027-2018>, 2018.](#)
- 1336 Lance, S., Brock, C. A., Rogers, D. and Gordon, J. A.: Water droplet calibration of the Cloud
1337 Droplet Probe (CDP) and in-flight performance in liquid, ice and mixed-phase clouds
1338 during ARCPAC, *Atmos. Meas. Tech.*, 3(6), 1683–1706, doi:10.5194/amt-3-1683-2010,
1339 2010.
- 1340 Latham, J. and Warwicker, R.: Charge transfer accompanying the splashing of supercooled
1341 raindrops on hailstones, *Q. J. R. Meteorol. Soc.*, 106(449), 559–568,
1342 doi:10.1002/qj.49710644912, 1980.
- 1343 Lauber, A., Kiselev, A., Pander, T., Handmann, P. and Leisner, T.: Secondary ice formation
1344 during freezing of levitated droplets, *J. Atmos. Sci.*, 75(8), 2815–2826, doi:10.1175/JAS-
1345 D-18-0052.1, 2018.
- 1346 Lauber, A., Henneberger, J., Mignani, C., Ramelli, F., Pasquier, J. T., Wieder, J., Hervo, M.
1347 and Lohmann, U.: Continuous secondary-ice production initiated by updrafts through the
1348 melting layer in mountainous regions, *Atmos. Chem. Phys.*, 21(5), 3855–3870,
1349 doi:10.5194/acp-21-3855-2021, 2021.
- 1350 Lawson, R. P., O’Connor, D., Zmarzly, P., Weaver, K., Baker, B., Mo, Q. and Jonsson, H.:
1351 The 2D-S (stereo) probe: Design and preliminary tests of a new airborne, high-speed, high-
1352 resolution particle imaging probe, *J. Atmos. Ocean. Technol.*, 23(11), 1462–1477,
1353 doi:10.1175/JTECH1927.1, 2006.
- 1354 Lawson, R. P., Woods, S. and Morrison, H.: The microphysics of ice and precipitation
1355 development in tropical cumulus clouds, *J. Atmos. Sci.*, 72(6), 2429–2445,
1356 doi:10.1175/JAS-D-14-0274.1, 2015.
- 1357 Lehning, M., I.Volksch, D.Gustafsson, Nguyen, T. A., Stahli, M. and Zappa, M.: ALPINE3D:
1358 A detailed model of mountain surface processes and its application to snow hydrology.,
1359 *Hydrol. Process.*, 20, 2111–2128, doi:10.1002/hyp.6204, 2006.
- 1360 Leisner, T., Pander, T., Handmann, P., and Kiselev, A.: Secondary ice processes upon
1361 heterogeneous freezing of cloud droplets, 14th Conf. on Cloud Physics and Atmospheric
1362 Radiation, Amer. Meteor. Soc, Boston, MA, 7 July 2014, available at:
1363 <https://ams.confex.com/ams/14CLOUD14ATRAD/webprogram/Paper250221.html> (last
1364 access: 9 November 2019), 2014.
- 1365 Lloyd, G., Choullarton, T. W., Bower, K. N., Gallagher, M. W., Connolly, P. J., Flynn, M.,
1366 Farrington, R., Crosier, J., Schlenzcek, O., Fugal, J. and Henneberger, J.: The origins of

1367 ice crystals measured in mixed-phase clouds at the high-alpine site Jungfraujoch, Atmos.
1368 Chem. Phys., 15(22), 12953–12969, doi:10.5194/acp-15-12953-2015, 2015.

1369 Lohmann, U., Henneberger, J., Henneberg, O., Fugal, J. P., Bühl, J. and Kanji, Z. A.:
1370 Persistence of orographic mixed-phase clouds, Geophys. Res. Lett., 43(19), 10,512-
1371 10,519, doi:10.1002/2016GL071036, 2016.

1372 Lowenthal, D. H., Hallar, A. G., David, R. O., Mccubbin, I. B., Borys, R. D. and Mace, G. G.:
1373 Mixed-phase orographic cloud microphysics during StormVEx and IFRACS, Atmos.
1374 Chem. Phys., 19(8), 5387–5401, doi:10.5194/acp-19-5387-2019, 2019.

1375 Luke, E. P., Yang, F., Kollias, P., Vogelmann, A. M. and Maahn, M.: New insights into ice
1376 multiplication using remote-sensing observations of slightly supercooled mixed-phase
1377 clouds in the Arctic, Proc. Natl. Acad. Sci. U. S. A., 118(13), 1–9,
1378 doi:10.1073/pnas.2021387118, 2021.

1379 Mahesh, A., Eager, R., Campbell, J. R. and Spinhirne, J. D.: Observations of blowing snow at
1380 the South Pole, J. Geophys. Res. Atmos., 108(22), 1–9, doi:10.1029/2002jd003327, 2003.

1381 Meyers, M. P., DeMott, P. J. and Cotton, W. R.: New Primary Ice-Nucleation
1382 Parameterizations in an Explicit Cloud Model, J. Appl. Meteorol., 31, 708–721,
1383 doi:10.1175/1520-0450(1992)031<0708:NPINPI>2.0.CO;2, 1992.

1384 Mignani, C., Creamean, J. M., Zimmermann, L., Alewell, C. and Conen, F.: New type of
1385 evidence for secondary ice formation at around -15 °c in mixed-phase clouds, Atmos.
1386 Chem. Phys., 19(2), 877–886, doi:10.5194/acp-19-877-2019, 2019.

1387 Morrison, H., Curry, J. A. and Khvorostyanov, V. I.: A new double-moment microphysics
1388 parameterization for application in cloud and climate models. Part I: Description, J. Atmos.
1389 Sci., 62, 1678–1693, doi:10.1175/JAS3446.1, 2005.

1390 Morrison, H. and Grabowski, W. W.: A novel approach for representing ice microphysics in
1391 models: Description and tests using a kinematic framework, J. Atmos. Sci., 65(5),
1392 doi:10.1175/2007JAS2491.1, 2008.

1393 Morrison, H., De Boer, G., Feingold, G., Harrington, J., Shupe, M. D. and Sulia, K.: Resilience
1394 of persistent Arctic mixed-phase clouds, Nat. Geosci., 5(1), 11–17, doi:10.1038/ngeo1332,
1395 2012.

1396 Mott, R., Scipión, D., Schneebeli, M., Dawes, N., Berne, A. and Lehning, M.: Orographic
1397 effects on snow deposition patterns in mountainous terrain, J. Geophys. Res., 119(3),
1398 1419–1439, doi:10.1002/2013JD019880, 2014.

1399 Müllmenstädt, J., Sourdeval, O., Delanoë, J. and Quaas, J.: Frequency of occurrence of rain
1400 from liquid-, mixed-, and ice-phase clouds derived from A-Train satellite retrievals,

1401 Geophys. Res. Lett., 42(15), 6502–6509, doi:10.1002/2015GL064604, 2015.

1402 Panziera, L. and Hoskins, B.: Large snowfall events in the south-eastern Alps, *Weather*, 63(4),
1403 88–93, doi:10.1002/wea.178, 2008.

1404 Phillips, V. T. J., Blyth, A. M., Brown, P. R. A., Choullarton, T. W. and Latham, J.: The
1405 glaciation of a cumulus cloud over New Mexico, *Q. J. R. Meteorol. Soc.*, 127(575), 1513–
1406 1534, doi:10.1256/smsqj.57502, 2001.

1407 Phillips, V. T. J., Yano, J. I. and Khain, A.: Ice multiplication by breakup in ice-ice collisions.
1408 Part I: Theoretical formulation, *J. Atmos. Sci.*, 74(6), 1705–1719, doi:10.1175/JAS-D-16-
1409 0224.1, 2017a.

1410 Phillips, V. T. J., Yano, J. I., Formenton, M., Ilotoviz, E., Kanawade, V., Kudzotsa, I., Sun, J.,
1411 Bansemer, A., Detwiler, A. G., Khain, A. and Tessorod, S. A.: Ice multiplication by
1412 breakup in ice-ice collisions. Part II: Numerical simulations, *J. Atmos. Sci.*, 74(9), 2789–
1413 2811, doi:10.1175/JAS-D-16-0223.1, 2017b.

1414 Phillips, V. T. J., Patade, S., Gutierrez, J. and Bansemer, A.: Secondary ice production by
1415 fragmentation of freezing drops: Formulation and theory, *J. Atmos. Sci.*, 75(9), 3031–
1416 3070, doi:10.1175/JAS-D-17-0190.1, 2018.

1417 Proske, U., Bessenbacher, V., Dedekind, Z., Lohmann, U. and Neubauer, D.: How frequent is
1418 natural cloud seeding from ice cloud layers ($<-35^{\circ}\text{C}$) over Switzerland?, *Atmos. Chem.*
1419 *Phys.*, 21(6), 5195–5216, doi:10.5194/acp-21-5195-2021, 2021.

1420 Pruppacher, H. R. and Klett, J. D.: *Microphysics of Clouds and Precipitation*, 2nd Edition,
1421 Kluwer Academic, Dordrecht, 954 pp., 1997.

1422 Purdy, J. C., Austin, G. L., Seed, A. W. and Cluckie, I. D.: Radar evidence of orographic
1423 enhancement due to the seeder feeder mechanism, *Meteorol. Appl.*, 12(3), 199–206,
1424 doi:10.1017/S1350482705001672, 2005.

1425 Qu, Y., Khain, A., Phillips, V., Ilotoviz, E., Shpund, J., Patade, S. and Chen, B.: The Role of
1426 Ice Splintering on Microphysics of Deep Convective Clouds Forming Under Different
1427 Aerosol Conditions: Simulations Using the Model With Spectral Bin Microphysics, *J.*
1428 *Geophys. Res. Atmos.*, 125(3), 1–23, doi:10.1029/2019JD031312, 2020.

1429 Ramelli, F., Henneberger, J., David, R., Bühl, J., Radenz, M., Seifert, P., Wieder, J., Lauber,
1430 A., Pasquier, J., Engelmann, R., Mignani, C., Hervo, M. and Lohmann, U.: Microphysical
1431 investigation of the seeder and feeder region of an Alpine mixed-phase cloud, *Atmos.*
1432 *Chem. Phys.*, 21, 6681–6706, doi:10.5194/acp-21-6681-2021, 2021.

1433 Rangno, A. L. and Hobbs, P. V.: Ice particles in stratiform clouds in the Arctic and possible
1434 mechanisms for the production of high ice concentrations, *J. Geophys. Res. Atmos.*,

1435 106(D14), 15065–15075, doi:10.1029/2000JD900286, 2001.

1436 Rasmussen, R. M., Geresdi, I., Thompson, G., Manning, K. and Karplus, E.: Freezing drizzle
1437 formation in stably stratified layer clouds: The role of radiative cooling of cloud droplets,
1438 cloud condensation nuclei, and ice initiation, *J. Atmos. Sci.*, 59(4), 837–860,
1439 doi:10.1175/1520-0469(2002)059<0837:FDFISS>2.0.CO;2, 2002.

1440 Reinking, R. F., Snider, J. B. and Coen, J. L.: Influences of storm-embedded orographic gravity
1441 waves on cloud liquid water and precipitation, *J. Appl. Meteorol.*, 39(6), 733–759,
1442 doi:10.1175/1520-0450(2000)039<0733:IOSEOG>2.0.CO;2, 2000.

1443 Reisner, J., Rasmussen, R. M. and Bruintjes, R. T.: Explicit forecasting of supercooled liquid
1444 water in winter storms using the MM5 mesoscale model, *Q. J. R. Meteorol. Soc.*, 124(548),
1445 1071–1107, doi:10.1002/qj.49712454804, 1998.

1446 Roe, G. H.: Orographic Precipitation, *Annu. Rev. Earth Planet. Sci.*, 33, 645–671,
1447 doi:10.1146/annurev.earth.33.092203.122541, 2005.

1448 Rogers, D. C. and Vali, G.: Ice Crystal Production by Mountain Surfaces, *J. Clim. Appl.*
1449 *Meteorol.*, 26, 1152–1168, doi:10.1175/1520-0450(1987)026<1152:ICPBMS>2.0.CO;2,
1450 1987.

1451 Rotunno, R. and Houze, R. A.: Lessons on orographic precipitation from the Mesoscale Alpine
1452 Programme, *Q. J. R. Meteorol. Soc.*, 133, 811–830, doi:10.1002/qj.67, 2007.

1453 Schlenczek, O., J. P. Fugal, K. N. Bower, J. Crosier, M. J. Flynn, G. Lloyd, and S. Borrmann,
1454 2014: Properties of pure ice clouds in an alpine environment. 14th Conf. on Cloud Physics,
1455 Boston, MA, Amer. Meteor. Soc. [Available online at
1456 [https://ams.confex.com/ams/14CLOUD14ATRAD/webprogram/Manuscript/Paper25030](https://ams.confex.com/ams/14CLOUD14ATRAD/webprogram/Manuscript/Paper250304/Schlenczek_et_al_2014_AMS_extended_abstract_klein.pdf)
1457 [4/Schlenczek_et_al_2014_AMS_extended_abstract_klein.pdf](https://ams.confex.com/ams/14CLOUD14ATRAD/webprogram/Manuscript/Paper250304/Schlenczek_et_al_2014_AMS_extended_abstract_klein.pdf).]

1458 Schmidt, R. A.: Measuring particle size and snowfall intensity in drifting snow., *Cold Reg. Sci.*
1459 *Technol.*, 9, 121–129, doi:10.1016/0165-232X(84)90004-1, 1984.

1460 Schwarzenboeck, A., Shcherbakov, V., Lefevre, R., Gayet, J. F., Pointin, Y. and Duroure, C.:
1461 Indications for stellar-crystal fragmentation in Arctic clouds, *Atmos. Res.*, 92(2), 220–228,
1462 doi:10.1016/j.atmosres.2008.10.002, 2009.

1463 [Sharma, V., Gerber, F., and Lehning, M.: Introducing CRYOWRF v1.0: Multiscale](#)
1464 [atmospheric flow simulations with advanced snow cover modelling, *Geosci. Model Dev.*](#)
1465 [Discuss., doi:10.5194/gmd-2021-231, in review, 2021.](#)

1466 Sotiropoulou, G., Sullivan, S., Savre, J., Lloyd, G., Lachlan-Cope, T., Ekman, A. M. L. and
1467 Nenes, A.: The impact of secondary ice production on Arctic stratocumulus, *Atmos. Chem.*
1468 *Phys.*, 20, 1301–1316, doi:10.5194/acp-20-1301-2020, 2020.

1469 Sotiropoulou, G., Vignon, E., Young, G., Morrison, H., O'Shea, S. J., Lachlan-Cope, T., Berne,
1470 A. and Nenes, A.: Secondary ice production in summer clouds over the Antarctic coast:
1471 An underappreciated process in atmospheric models, *Atmos. Chem. Phys.*, 21(2), 755–
1472 771, doi:10.5194/acp-21-755-2021, 2021a.

1473 Sotiropoulou, G., Ickes, L., Nenes, A. and Ekman, A.: Ice multiplication from ice–ice collisions
1474 in the high Arctic: sensitivity to ice habit, rimed fraction, ice type and uncertainties in the
1475 numerical description of the process, *Atmos. Chem. Phys.*, 21, 9741–9760,
1476 doi:10.5194/acp-21-9741-2021, 2021b.

1477 Sullivan, S. C., Hoose, C., Kiselev, A., Leisner, T. and Nenes, A.: Initiation of secondary ice
1478 production in clouds, *Atmos. Chem. Phys.*, 18(3), 1593–1610, doi:10.5194/acp-18-1593-
1479 2018, 2018a.

1480 Sullivan, S. C., Barthlott, C., Crosier, J., Zhukov, I., Nenes, A. and Hoose, C.: The effect of
1481 secondary ice production parameterization on the simulation of a cold frontal rainband,
1482 *Atmos. Chem. Phys.*, 18, 16461–16480, doi:10.5194/acp-18-16461-2018, 2018b.

1483 Takahashi, T., Nagao, Y. and Kushiyama, Y.: Possible High Ice Particle Production during
1484 Graupel–Graupel Collisions, *J. Atmos. Sci.*, 52, 4523–4527, 1995.

1485 Thompson, G., Rasmussen, R. M. and Manning, K.: Explicit Forecasts of Winter Precipitation
1486 Using an Improved Bulk Microphysics Scheme. Part I: Description and Sensitivity
1487 Analysis, *Mon. Weather Rev.*, 132, 519–542, doi:10.1175/1520-
1488 0493(2004)132<0519:EFOWPU>2.0.CO;2, 2004.

1489 Vali, G., Leon, D. and Snider, J. R.: Ground-layer snow clouds, *Q. J. R. Meteorol. Soc.*,
1490 138(667), 1507–1525, doi:10.1002/qj.1882, 2012.

1491 Vardiman, L.: The Generation of Secondary Ice Particles in Clouds by Crystal–Crystal
1492 Collision, *J. Atmos. Sci.*, 35, 2168–2180, doi:10.1175/1520-
1493 0469(1978)035<2168:TGOSIP>2.0.CO;2, 1978.

1494 Vignon, É., Alexander, S. P., DeMott, P. J., Sotiropoulou, G., Gerber, F., Hill, T. C. J.,
1495 Marchand, R., Nenes, A. and Berne, A.: Challenging and Improving the Simulation of
1496 Mid-Level Mixed-Phase Clouds Over the High-Latitude Southern Ocean, *J. Geophys. Res.*
1497 *Atmos.*, 126(7), 1–21, doi:10.1029/2020jd033490, 2021.

1498 Vionnet, V., Guyomarc'h, G., Naaim Bouvet, F., Martin, E., Durand, Y., Bellot, H., Bel, C.
1499 and Pugliese, P.: Occurrence of blowing snow events at an alpine site over a 10-year
1500 period: Observations and modelling, *Adv. Water Resour.*, 55, 53–63,
1501 doi:10.1016/j.advwatres.2012.05.004, 2013.

1502 Vionnet, V., Martin, E., Masson, V., Guyomarc'H, G., Naaim-Bouvet, F., Prokop, A., Durand,

1503 Y. and Lac, C.: Simulation of wind-induced snow transport and sublimation in alpine
1504 terrain using a fully coupled snowpack/atmosphere model, *Cryosphere*, 8(2), 395–415,
1505 doi:10.5194/tc-8-395-2014, 2014.

1506 Willmott, C. J., Robeson, S. M. and Matsuura, K.: A refined index of model performance, *Int.*
1507 *J. Climatol.*, 32(13), 2088–2094, doi:10.1002/joc.2419, 2012.

1508 Xu, L., Russell, L. M., Somerville, R. C. J. and Quinn, P. K.: Frost flower aerosol effects on
1509 Arctic wintertime longwave cloud radiative forcing, *J. Geophys. Res. Atmos.*, 118(23),
1510 13282–13291, doi:10.1002/2013JD020554, 2013.

1511 Yano, J. I. and Phillips, V. T. J.: Ice-Ice collisions: An Ice multiplication process in atmospheric
1512 clouds, *J. Atmos. Sci.*, 68(2), 322–333, doi:10.1175/2010JAS3607.1, 2011.

1513 Yano, J. I., Phillips, V. T. J. and Kanawade, V.: Explosive ice multiplication by mechanical
1514 break-up in ice-ice collisions: A dynamical system-based study, *Q. J. R. Meteorol. Soc.*,
1515 142(695), 867–879, doi:10.1002/qj.2687, 2016.

1516 Young, G., Lachlan-Cope, T., O’Shea, S. J., Dearden, C., Listowski, C., Bower, K. N.,
1517 Choularton, T. W. and Gallagher, M. W.: Radiative Effects of Secondary Ice Enhancement
1518 in Coastal Antarctic Clouds, *Geophys. Res. Lett.*, 46, 2312–2321,
1519 doi:10.1029/2018GL080551, 2019.

1520 Zhao, X. and Liu, X.: Global Importance of Secondary Ice Production, *Geophys. Res. Lett.*,
1521 doi:10.1029/2021GL092581, [2021+2021a](#).

1522 [Zhao, X. and Liu, X.: Relative importance and interactions of primary and secondary ice](#)
1523 [production in the Arctic mixed-phase clouds, *Atmos. Chem. Phys. Discuss.*,](#)
1524 [doi:10.5194/acp-2021-686, in review, 2021b](#).

1525 Zhao, X., Liu, X., Phillips, V. T. J. and Patade, S.: Impacts of secondary ice production on
1526 Arctic mixed-phase clouds based on ARM observations and CAM6 single-column model
1527 simulations, *Atmos. Chem. Phys.*, 21(7), 5685–5703, doi:10.5194/acp-21-5685-2021,
1528 2021.